Utilizing cylindrical and cubical specimens with edge notch to determine size-independent fracture quantities of rock materials

R. Ince, E. Eren
Firat University, Faculty of Engineering, Department of Civil Engineering, Elazig, Turkey
rince@firat.edu.tr, http://orcid.org/0000-0002-9837-8284
eeren@firat.edu.tr, http://orcid.org/0000-0001-5282-398X

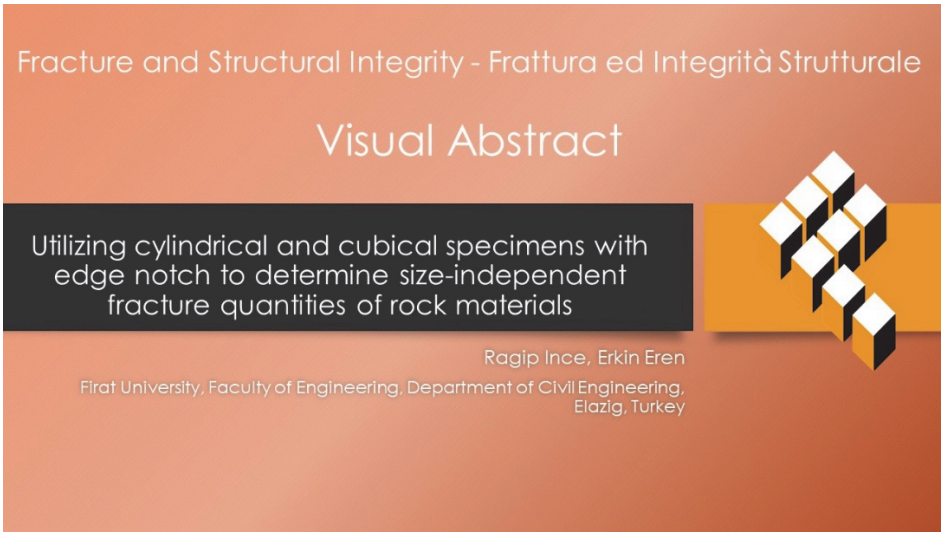

Citation: Ince, R., Eren, E., Utilizing cylindrical and cubical specimens with edge notch to determine size-independent fracture quantities of rock materials, Fracture and Structural Integrity, 75 (2026) 435-462.

Received: 04.10.2025
Accepted: 11.12.2025
Published: 11.12.2025
Issue: 01.2026

KEYWORDS. Crack Closure Integral (CCI), Double-K model, Single notched cube bend specimen, Straight-notched disk bend specimen, Two-parameter model (TPM).

INTRODUCTION

In materials science, clay products such as bricks, natural stones, and concrete are generally classified as ceramic materials. From ancient times to the present day, bricks and natural stones such as limestone, granite, and sandstone, as well as Roman concrete, have been widely used in buildings, bridges, and retaining walls. These materials are categorized as quite brittle in materials science, meaning that while their compressive strength is reasonable, their tensile strength is poor. Therefore, in practice, ceramic materials are simulated using the Mohr-Coulomb criterion, one of the classical fracture theories, where materials are assumed to be flawless. Moreover, bricks, natural stones, and concrete contain many voids, both open and closed.

In the 1920s, experimental research on brittle materials such as glass revealed that no material was perfect. Subsequently, the principle of linear elastic fracture mechanics (LEFM) was introduced. Irwin [1] improved this theory in the 1950s and proposed two equivalent material quantities, fracture toughness, and the critical strain energy release rate, to simulate

structures containing cracks. Irwin's approach was applied to concrete beams of different sizes in 1961 and observed that Irwin's material quantities were size-dependent for concrete. After the 1970s, experimental studies on the aforementioned ceramic materials revealed that these materials exhibit quasi-brittle failure, as a region containing a high density of microcracks, known as the fracture process zone (FPZ), can develop in the vicinity of the crack tip. In quasi-brittle materials, the initially sharp crack tip becomes blunted with increasing loading. As a result, failure in a cracked structure occurs only after the crack reaches a certain depth proportional to the FPZ, differing from truly brittle materials. Since 1976, various nonlinear fracture models, which employ at least two fracture quantities, have been developed to account for crack-tip blunting in quasi-brittle materials such as cementitious composites, rock, and asphalt [2–4].

The first applications of these fracture models focused on concrete and mortar materials. Until 1990, test results on rock material beams and compact tension (CT) specimens of various sizes revealed that the values of fracture toughness and the critical J-integral were independent of specimen width but dependent on specimen size. Considering this, a compliance technique commonly used in concrete fracture was first proposed for chevron bend specimens and short rod specimens to determine the nonlinear fracture toughness of rock materials by ISRM (International Society for Rock Mechanics) [5]. Bažant and Kazemi [3] successfully applied the size effect model (SEM) to experimental data obtained from beams and CT specimens of Hashida and Takahashi's Iidate granite. Bažant et al. [6] simulated the results of fracture tests on Indiana limestone beams of four different sizes using the SEM. Subsequently, Ouyang et al. [7] modeled Bažant and co-workers' [6] test results on Iidate granite using the two-parameter model (TPM).

Although beams and CT specimens containing cracks are widely used to determine fracture quantities of quasi-brittle materials and metals, the use of compact specimens, illustrated in Fig. 1, has recently become more common for cementitious materials, rock, and asphalt concrete. The wedge-splitting (WS) specimens and compact compression specimens, shown in Figs. 1a and 1b, were developed as alternatives to CT specimens and have been widely employed to determine the nonlinear fracture quantities of cementitious composites such as mortar and concrete. While splitting specimens in cylindrical and cubical forms have been widely used to indirectly evaluate the tensile strength of quasi-brittle materials, their centrally notched forms, shown in Fig. 1c, have also been applied to determine the nonlinear fracture quantities of cementitious materials. Ince [8] modeled edge-notched mortar cubes, which behave as splitting specimens, using the TPM (Fig. 1d). The semi-circular bending (SCB) specimens illustrated in Fig. 1e are the most commonly used samples in fracture testing of rock and asphalt materials since they can easily be produced from cylindrical core samples. Many fracture tests on SCB specimens have been conducted to evaluate the critical J-integral value and the LEFM-based fracture toughness of asphalt composites. Zegeye et al. [9] modeled asphalt SCB specimens of various sizes at low temperatures using the SEM. Ince et al. [10] initially derived some LEFM relationships regarding crack blunting in SCB specimens and subsequently simulated various SCB tests on asphalt from the literature using the TPM in concrete fracture. While many studies on rock SCB specimens have been performed based on LEFM by several researchers, other investigators have modeled rock materials by considering the nonlinear fracture behavior of these materials. Wei et al. [11] modeled SCB specimens containing a notch and chevron-notched SCB specimens using the finite element method. They then conducted fracture tests on Changtai granite specimens of three different depths and determined the nonlinear fracture toughness parameters using their equivalent elastic fracture model. Guo et al. [12] determined fracture quantities based on the SEM for granite SCB specimens of various sizes at room and high temperatures. Recently, Ince [13] conducted two series of experimental studies with SCB and beam specimens made of concrete and mortar and discussed them based on the three most popular fracture models: the TPM, the SEM, and the double-*K* model. Subsequently, three sets of SCB rock tests from the literature were analyzed using the aforementioned concrete fracture models, emphasizing that the nonlinear fracture quantities of both rock and concrete materials can be effectively assessed using single-sized SCB specimens.

Tutluoglu and Keles [14,15] derived the stress intensity factor (SIF) values for straight-notched disk bending (SNDB) specimens with different height-to-diameter ratios (Fig. 1f), a simplified form of the short rod specimen proposed by ISRM [5]. Subsequently, they conducted bending fracture tests on SNDB specimens, SCB specimens, and cracked chevron-notched Brazilian disks composed of andesite and marble to comparatively determine mode I fracture toughness. They proposed a numerical model to compute the fracture process zone (FPZ) depth of these stone materials and concluded that the FPZ depth of the SNDB specimen is smaller than that of other specimens. As a result, deviations from the assumptions of linear elastic fracture mechanics (LEFM) are reduced. In another study, Tutluoglu and co-workers [16] performed extensive experiments on andesite using SNDB specimens, SCB specimens, and three-point bending plates. Their results revealed that the critical normal strain value could be considered a material property across all tested specimen types. The aforementioned studies primarily focused on compact specimens subjected exclusively to pure mode I loading. Ayatollahi and Aliha [17] modeled both SCB specimens and splitting cylinders under mixed-mode loading using the finite element method.

In this study, SNDB specimens and single-notch cube bending (SNCB) specimens, cubic forms of SNDB specimens that differ from the edge-notched cube shown in Fig. 1d only in boundary conditions, were investigated both experimentally and numerically. First, a two-dimensional crack analysis of SNCB specimens was conducted using the finite element method (FEM) in ANSYS, determining SIF values, crack blunting expressions, and Green's functions. A three-dimensional crack analysis of SNCB specimens was also performed to obtain SIF values. Additionally, the existing SIF formulation for SNDB specimens with a diameter-to-height ratio of 2, originally developed by Tutluoglu and Keles [14], was refined based on this 3D analysis. Other LEFM equations, including crack blunting expressions and Green's functions, were also derived for SNDB specimens. Using these LEFM formulations, test data from Tutluoglu and Keles [14] were simulated using both the compliance method and the peak load method based on the two-parameter model (TPM), and the results were compared with the numerical model proposed by Tutluoglu and Keles [14]. A significant statistical correlation was observed between the three methods. Furthermore, fracture tests were conducted on Elazig limestone cubes with different edge crack depths but identical specimen sizes. The experimental results were analyzed using the peak load method with the SNCB specimen expressions. Consequently, this study emphasizes that, unlike the compliance approach, the nonlinear fracture properties of rock materials can be efficiently determined using the peak loads of single-sized cylindrical and cubic specimens with different edge-notch depths, eliminating the need for complex testing equipment.

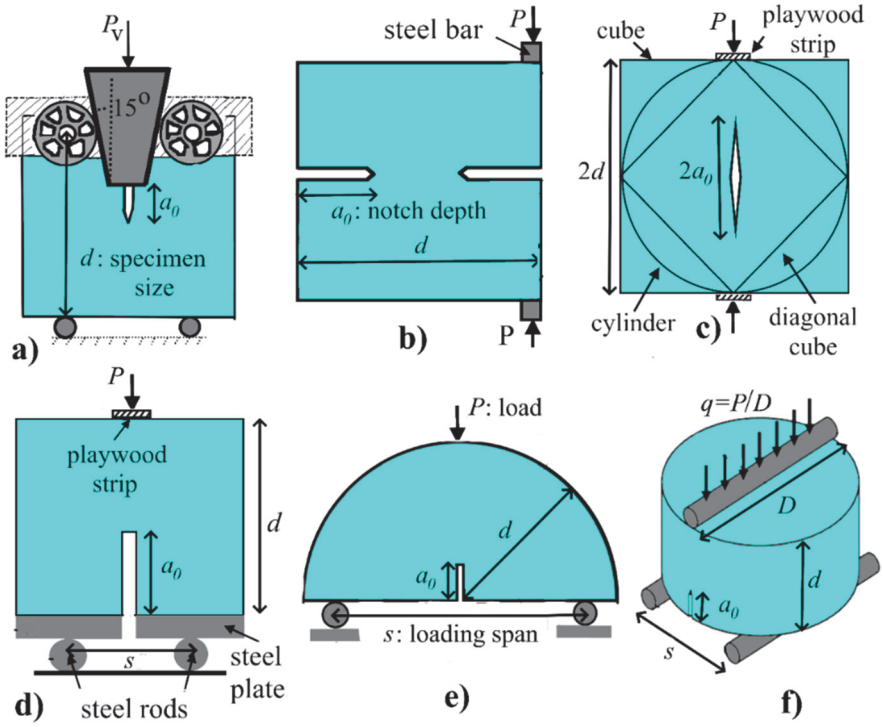

Figure 1: Notched compact specimens commonly used in testing of quasi-brittle materials a) WS specimen b) compact compression c) splitting specimens d) cube with edge notch e) SCB specimen f) SNDB specimen.

NON-LINEAR FRACTURE MODELS EMPLOYED IN THE MODELING OF QUASI-BRITTLE MATERIALS

Building elements consisting of quasi-brittle materials, such as rock and cement-based materials, exhibit a three-stage behavior until failure occurs. As seen in a beam with initial crack length a_0, whose load-crack mouth opening displacement relationship is presented in Fig. 2, these stages include: (1) crack initiation, corresponding to the range between the initial state and the first cracking load (P_i); (2) stable crack growth, corresponding to the range between the first cracking load and the peak load (P_c); and (3) unstable crack growth after the peak load. The beam, which behaves almost linearly elastic due to defects in the material until the first cracking load, exhibits non-linear behavior after this point due to the formation of a fracture process zone (FPZ) behind the free crack (Fig. 2c).

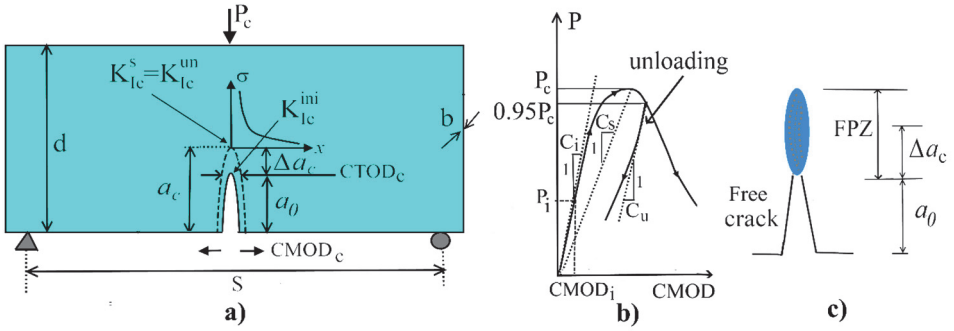

Figure 2: a) A typical quasi-brittle beam b) P-CMOD curve c) FPZ formation behind the crack

To fully characterize this multiphase behavior, cohesive crack models, which take into account the cohesive nature of the FPZ, simulate quasi-brittle structural members using the finite element method and the boundary element method. On the other hand, equivalent elastic fracture models, which consider only the behavior up to the peak load of the structural member, aim to predict the crack extension at the peak load (Δa_c), which is proportional to the FPZ depth, as illustrated in Fig. 2c [2–4]. It is emphasized that none of the above-mentioned fracture models employ a single fracture parameter, such as fracture toughness or fracture energy, contrary to classical LEFM.

Among the equivalent elastic fracture models, the two-parameter model (TPM) [2] predicts only the unstable crack growth at peak load in quasi-brittle structures by utilizing two critical quantities corresponding to the critical crack length ($a_c=a_0+\Delta a_c$): the fracture toughness (K_{Ic}^s) and the crack tip opening displacement value ($CTOD_c$), which describes the blunting at the crack tip well, as defined above:

$$K_{Ic}^s = \sigma_{Nc}\sqrt{\pi a_c}\,Y\left(\alpha_c = \frac{a_c}{d}\right) \tag{1}$$

$$CTOD_c = \frac{4\sigma_{Nc}a_c}{E}V_1\left(\alpha_c = \frac{a_c}{d}\right)M\left(\frac{a_0}{a_c}, \alpha_c = \frac{a_c}{d}\right) \tag{2}$$

Here, σ_{Nc} refers to the strength value computed according to the classical strength of materials theory for unnotched specimens, and it is commonly referred to as nominal strength. E in Eqn. (2) represents Young's modulus of the material. In Eqns. (1) and (2), the normalized functions Y, V_1, and M are based on crack lengths (a_0 and a_c) and the specimen depth (d). These functions can be computed from crack analysis by employing numerical methods such as the finite element method (FEM) for the specimen considered or may be found in LEFM books for simple specimen types. As an example, the normalized functions employed for beam specimens with span/depth=2.5, which are also used in this study, can be given below:

$$Y(\alpha) = \frac{1.83 - 1.65\alpha + 4.76\alpha^2 - 5.3\alpha^3 + 2.51\alpha^4}{\sqrt{\pi}\,(1+2\alpha)(1-\alpha)^{3/2}} \tag{3}$$

$$V_1(\alpha) = 0.65 - 1.88\alpha + 3.02\alpha^2 - 2.69\alpha^3 + \frac{0.68}{(1-\alpha)^2} \tag{4}$$

$$M\left(\frac{a_0}{a_c}, \alpha_c = \frac{a_c}{d}\right) = \sqrt{\left(1 - \frac{a_0}{a_c}\right)^2 + (1.081 - 1.149\alpha_c)\left[\frac{a_0}{a_c} - \left(\frac{a_0}{a_c}\right)^2\right]} \tag{5}$$

The double-*K* fracture model, based on equivalent elastic fracture models, simulates failure in quasi-brittle structures by utilizing two quantities: initiation and unstable fracture toughness (K_{Ic}^{un} and K_{Ic}^{ini}). Therefore, contrary to the TPM, both crack initiation and unstable crack growth in a quasi-brittle structure can be determined using Eqn. (1) through this model, where the values of a_0 and the first cracking load (P_i) are utilized to determine K_{Ic}^{un}.

As pointed out above, the only unknown points in Eqns. (1) and (2) are the critical (or effective) crack depth (a_c in the procedure for determining fracture quantities in the aforementioned fracture approaches. According to concrete fracture codes recommended by RILEM (International Union of Laboratories and Experts in Construction Materials, Systems and Structures), as illustrated in Fig. 2b, this critical quantity can be evaluated from the load–crack mouth opening displacement (P-CMOD) response of the test specimen (preferably a beam). However, to determine the P-CMOD response of the specimen, the use of a feedback-testing machine with CMOD control is necessary for the TPM, whereas no such requirement exists for the double-*K* model.

In approaches based on RILEM, Young's modulus (E) of the tested specimen is initially determined from the initial compliance value ($C_i=CMOD_i/P_i$), where P_i is commonly assumed to be $P_c/2$ due to difficulties in determining P_i (Fig. 2b). Subsequently, assuming that E remains constant for any pair of P and $CMOD$, the a_c value of the notched specimen is computed using the secant compliance value (C_s) in the double-*K* model or the unloading compliance value (C_u) in the TPM, as indicated in Fig. 2b. Although both models employ different test equipment and compliance techniques, experimental studies on beams and wedge-splitting specimens by Xu et al. revealed that the fracture toughness and $CTOD_c$ values obtained using the TPM were in good statistical agreement with those of the double-*K* model.

An alternative method, which utilizes only the ultimate loads of at least three specimens with different notch depths, was developed for the TPM by Tang et al. [18]. In this so-called peak-load method in concrete fracture, both fracture parameters (K_{Ic}^{s} and $CTOD_c$) are treated as unknowns instead of a_c values for the specimens. Consequently, this system, which consists of multiple equations but only two unknowns, can only be solved using an optimization-based approach. To achieve this, Tang et al. proposed that K_{Ic}^{s} and $CTOD_c$ curves corresponding to specific notch depths should first be determined for each specimen with a distinct a_0. The values of the sample standard deviation (s) corresponding to the same K_{Ic}^{s} value are then calculated using Eqn. (6):

$$s\left(K_{Ic}^{s}\right)=\sqrt{\sum_{i=1}^{n}\left(\overline{CTOD_c}-CTOD_{ci}\right)^2\Big/n-1},\qquad i=1,2,...,n \tag{6}$$

Here, $\overline{CTOD_c}$ is the mean value of $CTOD_{ci}$ values. Consequently, the K_{Ic}^{s} and $CTOD_c$ values, where $s\left(K_{Ic}^{s}\right)$ is at its minimum, are accepted as the fracture quantities according to the peak-load method.

As stated above, determining the initial cracking load (P_i) of the specimens is difficult. Therefore, Xu and Reinhardt [4] recommended a simplified approach, known as the inverse method in concrete fracture, as follows:

$$K_{Ic}^{ini}=K_{Ic}^{un}-K_{Ic}^{c} \tag{7}$$

Here, K_{Ic}^{c} refers to the cohesive fracture toughness. As depicted in Fig. 3a, K_{Ic}^{c} corresponds to the toughness value consisting of cohesive stresses assumed to occur along the critical crack extension line (Δa_c). According to the inverse method, this cohesive stress distribution is trapezoidal, such that the maximum value of this distribution is supposed to correspond to the tensile strength of the material (f_t) while its lower value, $\sigma_s(CTOD_c)$, is the stress value determined according to the chosen stress–crack tip opening displacement function (σ-w), as indicated in Fig. 3a. In many applications up to the peak load in concrete fracture, using a linear function, as shown in Fig. 3b, provides an adequate approach for σ-w [19]. The area under this function is equal to the fracture energy (G_f), which is converted to fracture toughness using Irwin's G-K relation: $G_f=\left(K_{Ic}^{un}\right)^2\Big/E$ [1,3]. On the other hand, the toughness value created by such a trapezoidal stress distribution at the crack tip can be calculated by integrating the toughness values created by the individual forces ($P=\sigma dx$) shown in Fig. 3c:

$$K_{Ic}^{c}=\int_{a_0}^{a_c}\frac{2\sigma\left(x/a_c\right)}{\sqrt{\pi\, a_c}}G\left(\gamma=\frac{x}{a_c},\alpha=\frac{a_c}{d}\right)dx \tag{8}$$

Here, x refers to the vertical distance from the crack mouth of the specimen, and G is Green's function. For instance, Tada et al. [20] derived the following Green's function for an infinite strip as shown in Fig. 3c:

$$G(\gamma,\alpha)=\frac{3.52(1-\gamma)}{\left(1-\alpha^2\right)^{1.5}}-\frac{4.35-5.28\gamma}{(1-\alpha)^{0.5}}+\left[\frac{1.3-0.3\gamma^{1.5}}{\left(1-\gamma^2\right)^{0.5}}+0.83-1.76\gamma\right]\left[1-\alpha(1-\gamma)\right] \tag{9}$$

The results of the experiments on compact quasi-brittle samples by Ince [21] indicated that the fracture quantities (K_{Ic}^{un} and K_{Ic}^{ini}) of the double-K model can also be evaluated using the peak-load method.

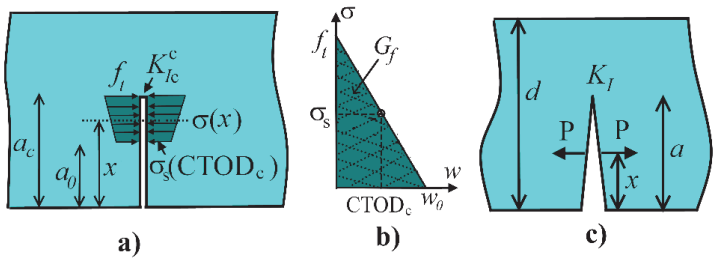

Figure 3: Computing of K_{Ic}^{c} according to the inverse method a) distribution of cohesive stress at peak load b) linear function for σ-w c) a body containing crack under wedge forces

DERIVATION OF FRACTURE MECHANICS FORMULAS OF SNDB AND SNCB SPECIMENS

Two prominent energy methods based on the FEM, such as the J-integral and the crack closure integral (CCI) technique[22], which can also be successfully utilized for three-dimensional crack problems, were employed in this study. Although conventional methods commonly used in FEM crack problems, such as extrapolation methods based on stress matching, displacement matching, and the hybrid method, require a large number of fine elements near a crack for accurate results, the aforementioned methods do not have such refined mesh requirements. The J-integral is a contour integral evaluated along a path that encircles the crack tip, beginning and concluding at the surfaces of the crack. Since this integral is path-independent for any of the contours, it has the same value for any similar contour. The use of the CCI technique is not as widespread as the J-integral approach and is not embedded in many commercial FEM programs, but the implementation of the CCI technique is very simple compared to the J-integral method, as will be detailed below.
The basic principles of the crack closure integral (CCI) technique can be derived using the fundamental principle of LEFM [1]. To determine the relationship between the energy release rate G and the fracture toughness K, it is necessary to account for the work of the closing forces ($P=\sigma dx$), which corresponds to the initial state of the new crack profile when a crack of length a increases by a small amount (Δa), as shown in Fig. 4a. For a plate with a thickness of b, the energy released as a result of the small extension of the crack ($Gb\Delta a$) must be equal to the work done by the internal forces that closed it. Accordingly, the following equation can be written:

$$W=\int_0^{\Delta a}\frac{1}{2}\sigma v dx=Gb\Delta a \tag{10}$$

Here, v is the crack opening displacement (COD). The above work expression can easily be applied by running two-step computer numerical approaches, such as the finite element method, where the elastic body model is assumed to be

continuous only at the selected nodes. To calculate the crack closure work in the body modeled with the linear plane finite elements, as shown in Fig. 4b, the nodal force at the crack tip (P_i) is determined for the original crack profile in the first step. Subsequently, the node at the crack tip is released, and the nodal displacement (v_i) is determined for the extended crack profile in the second step. On the other hand, when sufficiently small linear elements are used, the simple work equation, which can also be computed by utilizing the displacement value at the node just before the crack tip (v_{i-1}), could be obtained within acceptable limits by running a single step as follows ($W(a) \approx W(a+\Delta a)$):

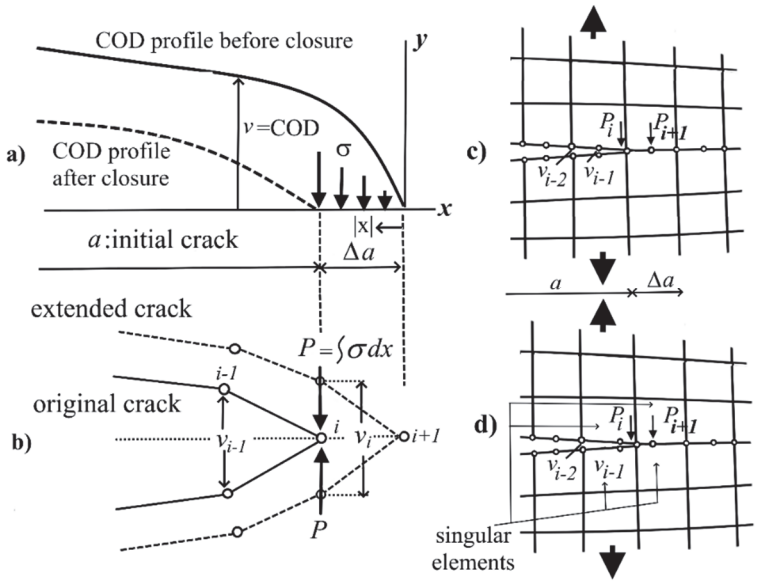

Figure 4: a) Crack closure stresses occurring behind the crack tip b) CCI technique in FEM with linear elements c) crack-tip discretization by plane elements with 8 nodes d) singular crack-tip discretization with 8 nodes [22].

$$W = \frac{1}{2} P_i v_i \approx \frac{1}{2} P_i v_{i-1} \tag{11}$$

Consequently, G and K can be determined for a cracked body modeled with linear plane finite elements by utilizing Eqns. (10) and (11) as follows:

$$G = \frac{K^2}{E} = \frac{P_i v_{i-1}}{2b\Delta a} \tag{12}$$

Similarly, as depicted in Fig. 4c and Fig. 4d, in elastic crack problems where 8-node plane elements with or without singular are used, G (and hence K) can be calculated as follows, respectively.

$$G = \frac{v_{i-1}}{2b\Delta a}\left[P_{i+1} + (1.5\pi - 4) P_i \right] \tag{13}$$

$$G = \frac{P_i v_{i-2} + P_{i+1} v_{i-1}}{2b\Delta a} \tag{14}$$

In this study, SNCB and SNDB specimens were simulated as deep beams subjected to three-point bending. While Tutluoglu and Keles [14] modeled SNDB specimens, as shown in Fig. 1f, they applied the external load to the specimen through rigid shell elements with an arch shape. However, Tang [23] revealed that the width of the distributed load has an insignificant effect on structures under three-point bending. Recently, Ince et al. [10] simulated semi-circular bending (SCB) specimens for asphalt concrete and concluded that this effect may also be ignored for SCB specimens. For instance, the relative error

between concentrated loading and distributed loading was smaller than 0.7% in the computations of the SIFs of SCB specimens.

In this study, the SNCB specimen illustrated in Fig. 5a was initially analyzed using 8-noded plane elements. Because of the symmetry of the specimen, half of it, with a depth of d=100 mm and a width of b=1 mm, was considered in the modeling, as shown in Fig. 5b. The specimen was discretized into 100 finite elements to minimize computation errors along the notch line. Furthermore, a total of eight quarter-point elements with six nodes were employed to consider the stress singularity around the notch. Note that Ince [21] previously utilized the same discretization along the notch line to model split-tension cylinders containing central cracks, for which an analytical solution was available. Consequently, it was observed that this discretization provided an accuracy of 0.2%.

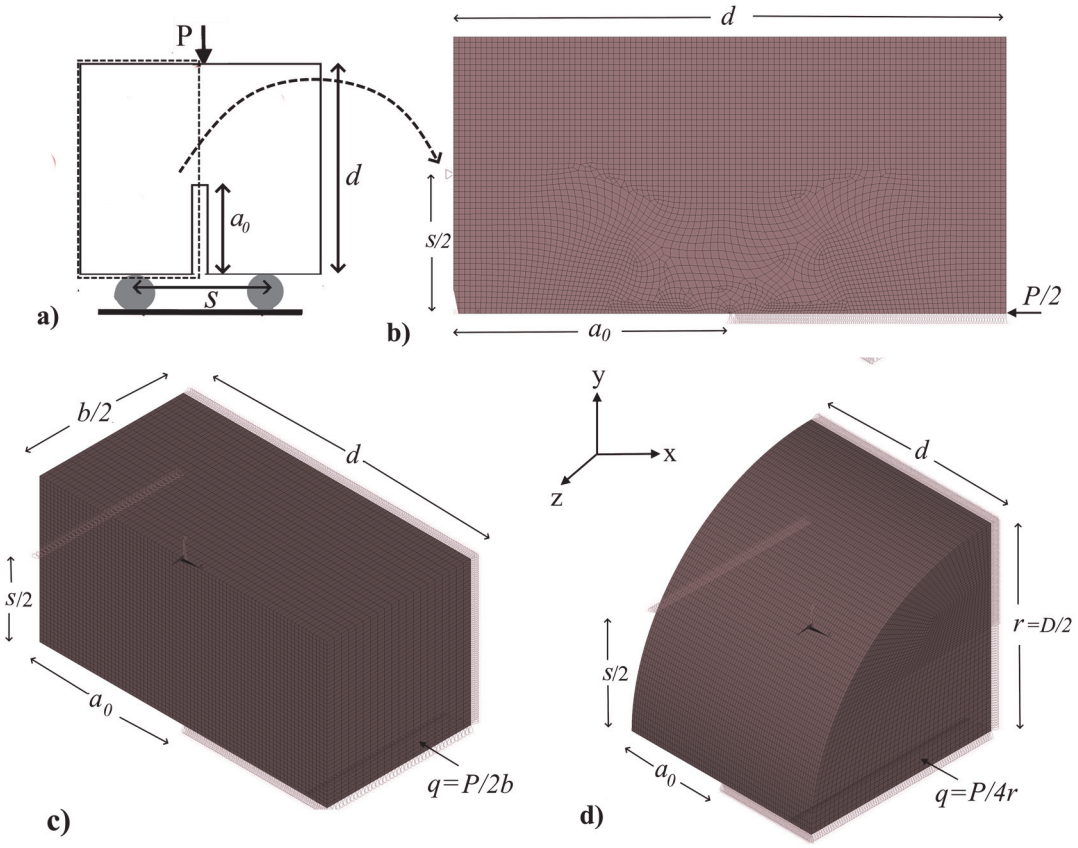

Figure 5: FEM discretization of simulated specimens a) characteristics of SNCB specimen b) 2D-SNCB modelling c) 3D-SNCB modelling d) SNDB modelling.

In the finite element analysis (FEA) by using ANSYS Parametric Design Language (APDL), the elastic constants of the material, elasticity modulus (E) and Poisson's ratio (ν), were selected as 1.0 MPa and 0.2, respectively, and the concentrated load (P) at the mid-span was set to 100 N. The relative notch depths ($\alpha_0=a_0/d$) were varied between 0.1 and 0.9 with a step interval of 0.1, while span-to-depth (s/d) ratios were chosen as 0.5, 0.6, 0.7, and 0.8. The normalized function (Y), based on the SIF of the SNCB specimen, was computed using both the J-integral and the CCI technique based on Eqn. (13) for each α_0 value. In this procedure, the value of the nominal strength (σ_N) in Eqn. (1) was taken as $P/(2bd)$, which was previously used for the SCB specimens and SNDB specimens by Tutluoglu and Keles [14]. In above 2D FEA, the type of PLANE183 elements in ANSYS element library (8-noded isoparametric element) were utilized except around the crack, where 8 quarter-point elements (6-noded singular elements) were used to account for the stress singularity at the crack tip.

To simulate the SNDB specimen reliably, the SNCB specimen was also modeled in 3D. For this, a quarter of the SNCB specimen was considered due to the symmetry of the cubic geometry (b=100 mm), as indicated in Fig. 5c. The 3D SNCB specimen containing a notch was modeled using both 8-noded (SOLID185) and 20-noded (SOLID186) solid elements without singular finite elements. In FEA, the elastic constants of the material were chosen as in the 2D analysis, while the concentrated load (P=100 N) at the mid-span was distributed along the specimen width, as depicted in Fig. 5c. The Y values

of the 3D SNCB specimens were calculated using the J-integral and the CCI technique for each α_0 and s/d ratio selected above. These values were determined for each finite element at the crack tip in the model with 20 nodes, whereas they were computed at the side surface of each finite element at the crack tip in the model with 8 nodes. In the crack analysis based on the CCI approach, Eqns. (12) and (14) were employed for the models with 8-noded and 20-noded solid elements, respectively.

In Fig. 6a, the Y values computed for α_0=0.5 are illustrated for s/d=0.5, 0.6, and 0.8 according to each solid element type. It is observed from Fig. 6a that there is a very close coincidence between both calculation methods, except for finite elements at the boundary of the specimen. The mean values, excluding the boundary values of the CCI technique, were also plotted according to both crack analyses in Fig. 6a. Based on this, it can be concluded that the solutions with 8-node elements are sufficiently compatible with those of 20-node elements.

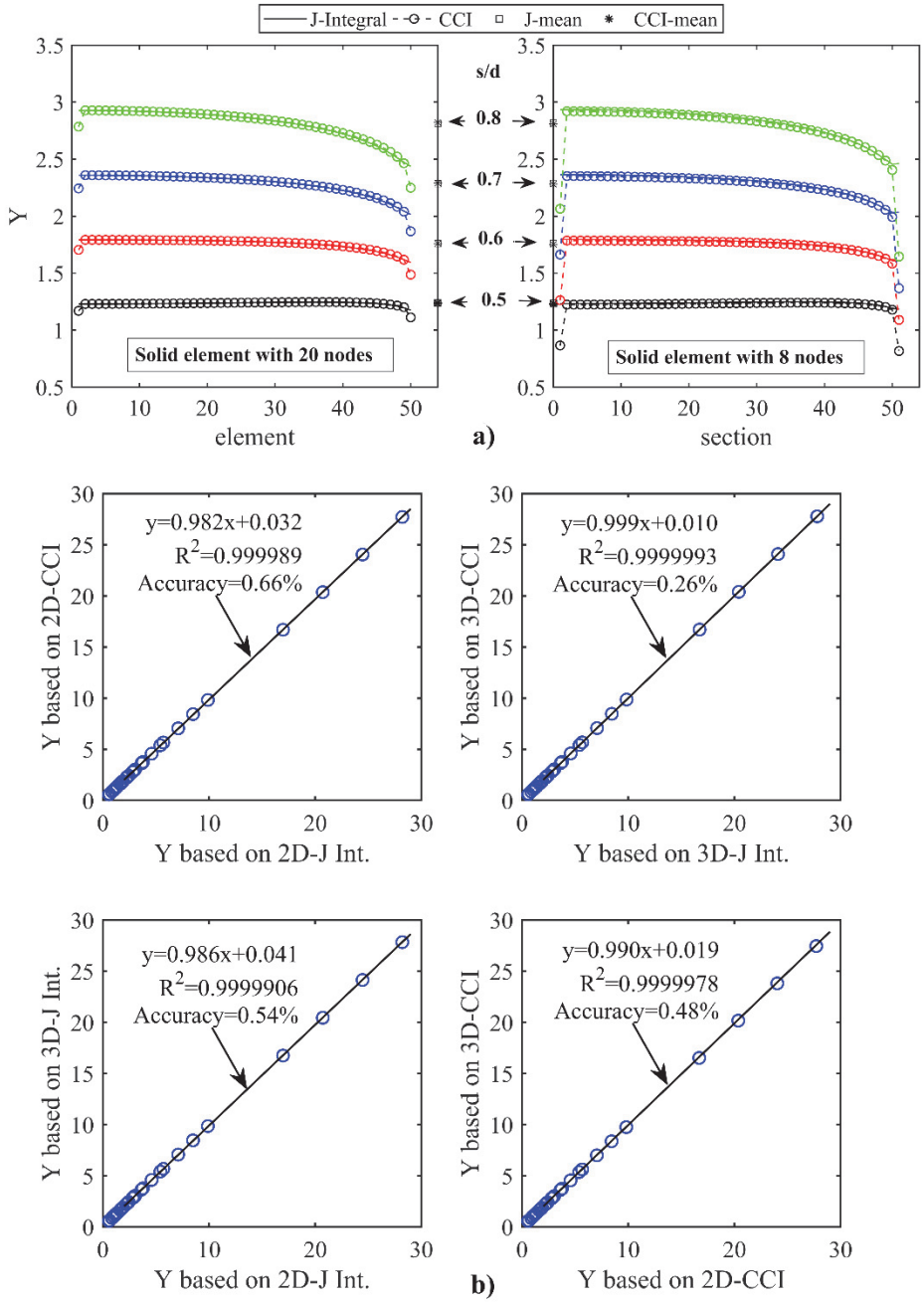

Figure 6: a) Y distribution along the section in 3D SNCB specimens with α=0.5 b) Comparison of 2D and 3D FEA for SNCB specimen.

Fig. 6b shows the FEA results of both 2D SNCB specimens with 8 nodes and 3D SNCB specimens with 20 nodes for all α_0 and s/d values considered, comparatively. The equations of the regression line ($Y=AX+C$), the determination coefficients (R^2) corresponding to these equations, and the maximum relative error (accuracy) computed for each data point were also reported in this figure. In an ideal model, the parameters A, C, and R^2 should attain values of 1, 0, and 1, respectively. It can be seen from this figure that the results of the SNCB models based on 2D and 3D were satisfactorily consistent according to the J-integral way and the CCI technique.

Based on the information above, the SNDB specimens with only a depth-to-diameter ratio (d/D) of 0.5 were simulated under the same conditions as the SNCB specimens for four different s/d ratios: 0.25, 0.30, 0.35, and 0.4. The FEM discretization of the quarter part of the SNDB specimen is illustrated in Fig. 5d.

In this study, the results of 2D FEA were used while deriving the following LEFM formulas for the SNCB specimens. According to the FEM discretization in Fig. 5b, in addition to the SIF, the vertical displacement values at each node along the crack were recorded to determine the COD profile of the SNCB specimen. This procedure was also performed along the cylinder axis for the SNDB specimen. Note that the maximum COD value is equal to the CMOD value.

Similar to the beam with span/depth=2.5 (Eqn. (3)), the following formulas were selected for the general form of Y for the SNDB specimen and the SNCB specimen, respectively.

$$Y\left(\alpha=\frac{a}{d}\right)=\frac{A_0+A_1\alpha+A_2\alpha^2+A_3\alpha^3+A_4\alpha^4}{(1+2\alpha)(1-\alpha)^{1.5}} \tag{15}$$

$$Y\left(\alpha=\frac{a}{d}\right)=\frac{A_0+A_1\alpha+A_2\alpha^2+A_3\alpha^3+A_4\alpha^4+A_5\alpha^5}{(1+2\alpha)(1-\alpha)^{1.5}} \tag{16}$$

The normalized equations for Y in Eqns. (15) and (16) were calculated by normalizing the FEM computations-based K_I values with the values of $(P\sqrt{(\pi a_0)}/2bd)$ for each specimen geometry, a/d, and span/depth ratio. In Tab. 1, the regression coefficients (A_i) computed using the least squares method are tabulated for each specimen geometry and span/depth ratio. The maximum relative error (accuracy) between the individual FEA analysis data and the above regression formulas was obtained as 0.2% and 0.3% for Eqns. (15) and (16), respectively.

According to the mechanics of structures containing cracks, the displacement expressions of a cracked structure, such as CMOD, depend on both the elastic constants (E and ν) of the material and the characteristic size of the structure. Consequently, a general expression of CMOD that satisfies boundary conditions was chosen as follows:

$$CMOD=\frac{Pa}{2bE}V_1(a) \tag{17}$$

$$V_1(a)=B_0+B_1a+B_2a^2+B_3a^3+\frac{B_4}{(1-a)^2} \tag{18}$$

Similar to beam (Eqn. (4)), the following two formulas were selected for the dimensionless V_1 function of the SNDB specimen and the SNCB specimen, respectively:

$$V_1(a)=B_0+B_1a+B_2a^2+B_3a^3+B_4a^4+\frac{B_5}{(1-a)^2} \tag{19}$$

The regression coefficients (B_i) corresponding to the above equations are reported for each specimen geometry and s/d ratio in Tab. 1. Eqns. (18) and (19) are valid for $0.1\leq\alpha_0\leq0.9$ within 0.5% and 0.4% accuracy, respectively. The dimensionless functions derived for cylindrical and cubical specimens are represented by the curved line for $0.1\leq\alpha_0\leq0.8$ in Fig. 7, as the values for $\alpha_0=0.9$ are too high. In the same figure, several values determined by Tutluoglu and Keles [14] are also plotted using + markers. It can be seen from this figure that the results of Eqn. (15) exhibit satisfactory accuracy. Note that 95% confidence interval (CI) values (CI-L lower and CI-U upper) were also presented for each coefficient in Tab. 1.

Spec.	s/D	s/d	Coef.	0	1	2	3	4	5
			A_i	3.516	-7.146	15.045	-11.268	3.139	
	0.5	0.25	CI-L	3.487	-7.464	13.972	-12,692	2.492	
			CI-U	3.545	-6.829	16.119	-9.846	3.787	
			A_i	3.936	-5.304	10.031	-5.659	0.927	
	0.6	0.30	CI-L	3.915	-5.526	9.282	-6.653	0.475	
			CI-U	3.956	-5.083	10.780	-4.666	1.379	
			A_i	4.408	-4.119	7.121	-2.597	-0.232	
	0.7	0.35	CI-L	4.373	-4.495	5.852	-4.280	-0.997	
			CI-U	4.442	-3.744	8.391	-0.914	0.534	
SNDB			A_i	4.905	-3.182	4.627	0.392	-1.565	
	0.8	0.40	CI-L	4.832	-3.978	1.934	-3.178	-3.189	
			CI-U	4.979	-2.385	7.321	3.962	0.059	
			B_i	10.819	-28.272	38.965	-33.829	7.464	
	0.5	0.25	CI-L	10.678	-29.608	35.491	-36.530	7.461	
			CI-U	10.960	-26.936	42.440	-31.129	7.466	
			B_i	12.559	-27.789	36.435	-27.679	9.029	
	0.6	0.30	CI-L	12.331	-29.951	30.815	-32.048	9.025	
			CI-U	12.788	-25.628	42.055	-23.310	9.033	
			B_i	15.105	-30.183	37.261	-22.530	10.595	
	0.7	0.35	CI-L	14.529	-35.637	23.080	-33.554	10.585	
			CI-U	15.681	-24.729	51.442	-11.505	10.605	
			B_i	18.059	-31.357	30.702	-8.206	12.069	
	0.8	0.40	CI-L	16.789	-43.382	-0.566	-32.514	12.046	
			CI-U	19.329	-19.332	61.970	16.102	12.091	
			A_i	2.448	-20.906	82.673	-146.001	123.619	-40.248
		0.5	CI-L	2.186	-24.880	62.629	-190.470	78.705	-57.137
			CI-U	2.710	-16.933	102.717	-101.533	168.532	-23.358
			A_i	2.854	-16.967	60.766	-102.025	84.581	-27.245
		0.6	CI-L	2.759	-18.442	53.325	-188.535	67.906	-33.515
			CI-U	2.951	-15.492	68.208	-85.515	101.256	-20.974
			A_i	3.222	-13.133	40.903	-64.107	52.378	-16.933
		0.7	CI-L	3.183	-13.725	37.918	-70.731	45.688	-19.449
			CI-U	3.261	-12.541	43.889	-57.484	59.068	-14.418
SNCB			A_i	3.672	-10.172	24.706	-33.460	26.953	-9.015
		0.8	CI-L	3.619	-10.978	20.640	-42.480	17.843	-12.441
			CI-U	3.725	-9.366	28.772	-24.440	36.064	-5.589
			B_i	8.050	-40.143	28.182	56.025	-93.908	3.674
		0.5	CI-L	7.031	-53.859	-30.674	-42.544	-150.843	3.654
			CI-U	9.069	-26.426	87.037	154.596	-36.974	3.694
			B_i	8.691	-27.460	5.715	74.589	-101.024	4.476
		0.6	CI-L	7.744	-40.216	-49.017	-17.077	-153.970	4.458
			CI-U	9.638	-14.704	60.448	166.255	-48.077	4.495
			B_i	9.835	-20.807	4.416	63.861	-93.876	5.276
		0.7	CI-L	8.833	-34.312	-53.534	-33.190	-149.935	5.257
			CI-U	10.838	-7.301	62.364	160.915	-37.819	5.296
			B_i	11.578	-17.613	13.057	40.423	-80.801	6.075
		0.8	CI-L	10.480	-32.405	-50.409	-65.868	-142.196	6.054
			CI-U	12.677	-2.822	76.522	146.716	-19.407	6.097

Table 1: The coefficients and confidence interval (CI) values of regression of SNDB and SNCB specimens.

The COD/CMOD ratio depends on the structure's geometry and loading type but is independent of its size. When this ratio is known for any structure, the critical value of CTOD for the material can be easily determined. Consequently, Eqns. (20) and (21) were selected as the COD profiles for the SNDB specimen and the SNCB specimen, respectively:

$$\frac{COD(y)}{CMOD}=\sqrt{\left(1-\frac{y}{a}\right)^2+\left(0.981-1.361\alpha+0.377\alpha^2\right)\left[\frac{y}{a}-\left(\frac{y}{a}\right)^2\right]} \tag{20}$$

$$\frac{COD(y)}{CMOD}=\sqrt{\left(1-\frac{y}{a}\right)^2+\left(1.007-2.747\alpha+2.018\alpha^2\right)\left[\frac{y}{a}-\left(\frac{y}{a}\right)^2\right]} \tag{21}$$

Consequently, the $CTOD_c$ value for the material can be computed using the values $y=a_0$, $a=a_c$ and $\alpha=a_c/d$. For all chosen values, Eqns. (20) and (21) achieve an accuracy better than 3.3%.

The validity of the above simulations performed was demonstrated in Fig. 8. Two mesh convergence plots for both 2D and 3D cases vs element size (1 mm, 2.5 mm, and 5 mm) were illustrated for a=0.1, 0.3, 0.5, 0.7, and 0.9 for SNCB specimens with s/d=0.8 in Fig. 8a. It is clearly seen from the figure that mesh structures with element sizes of 1 mm and 2.5 mm (corresponding to 100 and 40 elements along the crack line, respectively) gave very close results. In these comparisons, the maximum relative error calculated between 1 mm and 2.5 mm meshes was calculated as 1.3% for 2D mesh and 1.4% for 3D mesh, respectively, while these errors were 11.7% and 7.9% for the comparison between 1 mm and 5 mm meshes. As a result, it can be concluded that, as mentioned above, using 100 finite elements along the notch line is sufficient to minimize calculation errors. In Fig. 8b, the distributed load effect was investigated for the SNDB specimen. It is clearly seen from the figure that the relative errors between concentrated loading and distributed loading were smaller than 0.2% and 1.6% for ratios of the width of the distributed load to the specimen depth b=0.05 and 0.10, respectively. As mentioned above, this effect may be ignored for bending specimens. Fig. 8c presents contour plots with various radii (r) and corresponding Y values computed to show path independence for the J-integral of the 2D-SNCB specimen with a/d=0.5. Since the differences for the Y values are very small here, it can be said that the calculated J-integrals are path independent.

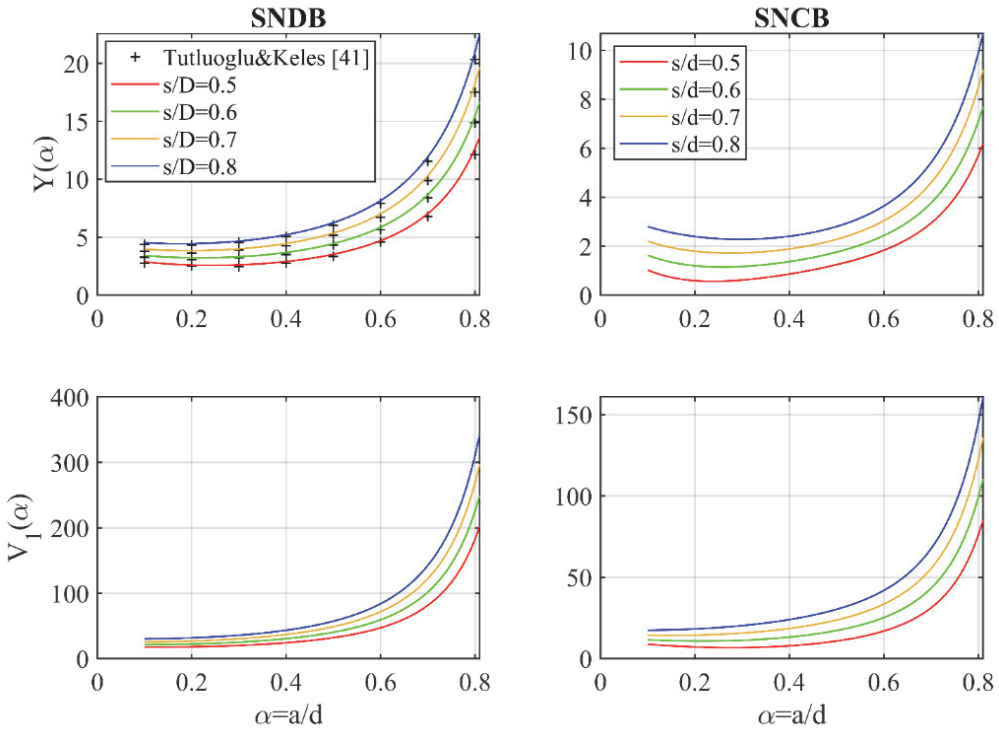

Figure 7: Dimensionless functions obtained from the FEA.

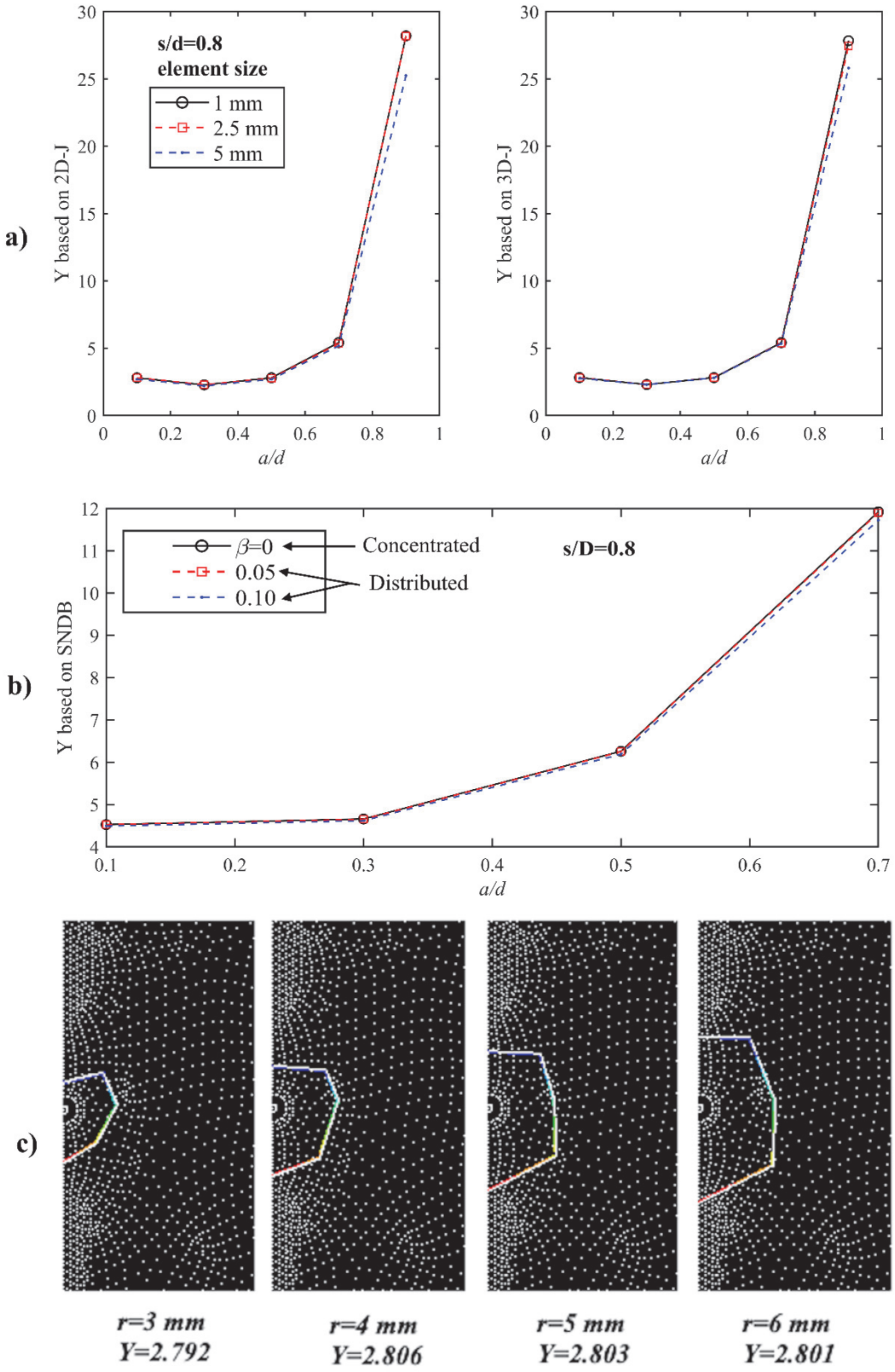

Figure 8: Validation check of simulations conducted a) Mesh convergence of SNCB specimen for 2D and 3D computations b) Distributed load effect for SNDB specimen c) Contour plots for J-integral for various contours showing path independence for 2D-SNCB specimen (a/d=0.5).

Deriving Green's functions for SNDB and SNCB specimens

The most important application of Green's function in Hookean structures, initially proposed by George Green in 1828 to model the response of a system to an impulse, is to estimate the stress field in response to a force acting at a point in the structure. For a cracked structure, the stress intensity factor (SIF, K) that occurs at the crack tip in response to a point force can be considered a special case of Green's function. For a body with a notch of depth a, subjected to Mode-I loading, K_I based on the Green's function, $G(x,a)$, can be described as follows:

$$K_I = \frac{2}{\sqrt{\pi a}} \int_0^a \sigma(x) G(x,a)\, dx \tag{22}$$

Here, $\sigma(x)$, for $0 \le x \le a$, represents the normal stress distribution function at the crack site for the structure without a crack due to external loads. According to Eqn. (22), a cracked structure can be analyzed as if it were the same structure devoid of external forces, where the relevant stresses are applied directly to the crack surface. In other words, once Green's function is obtained for any structure, instead of modeling the cracked structure, it is sufficient to solve the above integral based on the stress distribution along the crack line. Green's functions in the literature, primarily for two-dimensional elastic solids, have been derived analytically for strips, infinite sheets, and simple geometries such as disks. However, to address practical issues effectively, some form of approximation of the real problem requires numerical methods such as FEM.

FEM analysis performed in this study revealed that not only the SIF, as shown in Fig. 6a, but also the stress distribution varies across the cross-section of SNDB specimens subjected to bending. Therefore, to obtain a uniform stress distribution across the cross-section of an SNDB specimen, the SNDB specimen subjected to the hoop (or circumferential) stress (σ_0), as shown in Fig. 9a, was considered for determining the Green's function. Consequently, by employing the FEM discretization in Fig. 5d, the SIFs of SNDB specimens were determined for $0.1<\alpha=a/d<0.9$ using Eqn. (22). Similarly, SNCB specimens without a notch were initially modeled according to the FEM discretization in Fig. 5b under a uniform tensile stress (σ_0) for $0.1<\alpha=a/d<0.9$, as shown in Fig. 9b.

The expression described in Eqn. (9), which is employed for bending members, was used as the basis for Green's functions of the SNDB and the SNCB specimens because boundary conditions of the specimens examined in this study provide for $G(\alpha \to 0) = 1.3 - 0.3\gamma^{1.5}$ and $G(\alpha \to 1) = 3.52(1-\gamma)\Big/\sqrt{1-\gamma^2}$. Consequently, the remaining coefficients of Eqn. (9) (1.82, -1.39, -2.65, and 3.86) were adjusted to be suitable for each specimen geometry, such that Eqn. (22) was integrated with the stress function $\sigma(x)$, obtained from the FEM analysis for the specimen without a crack, to determine the Green's functions. The integration procedures in Eqn. (22) were performed using the Gauss-Chebyshev approach, while the Levenberg–Marquardt method was employed to compute the remaining coefficients. Therefore, for the SNDB and SNCB specimens, the derived Green's functions were:

$$G(\gamma,\alpha) = \frac{3.52(1-\gamma)}{\left(1-\alpha^2\right)^{1.5}} - \frac{0.73+0.86\gamma}{(1-\alpha)^{0.5}} + \left[\frac{1.3-0.3\gamma^{1.5}}{\left(1-\gamma^2\right)^{0.5}} - 7.35 + 12.78\gamma\right]\left[1-\alpha(1-\gamma)\right] \tag{23}$$

$$G(\gamma,\alpha) = \frac{3.52(1-\gamma)}{\left(1-\alpha^2\right)^{1.5}} - \frac{3.43-6.7\gamma}{(1-\alpha)^{0.5}} + \left[\frac{1.3-0.3\gamma^{1.5}}{\left(1-\gamma^2\right)^{0.5}} + 0.8 - 5.55\gamma\right]\left[1-\alpha(1-\gamma)\right] \tag{24}$$

For $0.1<\alpha=a/d<0.9$ and any $\gamma=x/a$, the accuracies of the above regression expressions were computed as 2.7% (R^2= 0.9999932) and 3.8% (R^2= 0.999778) for SNDB and SNCB, respectively, according to the individual FEM results. Fig. 9c illustrates the residuals as a percentage for the regression fits obtained for Green's functions in Eqns. (23) and (24).

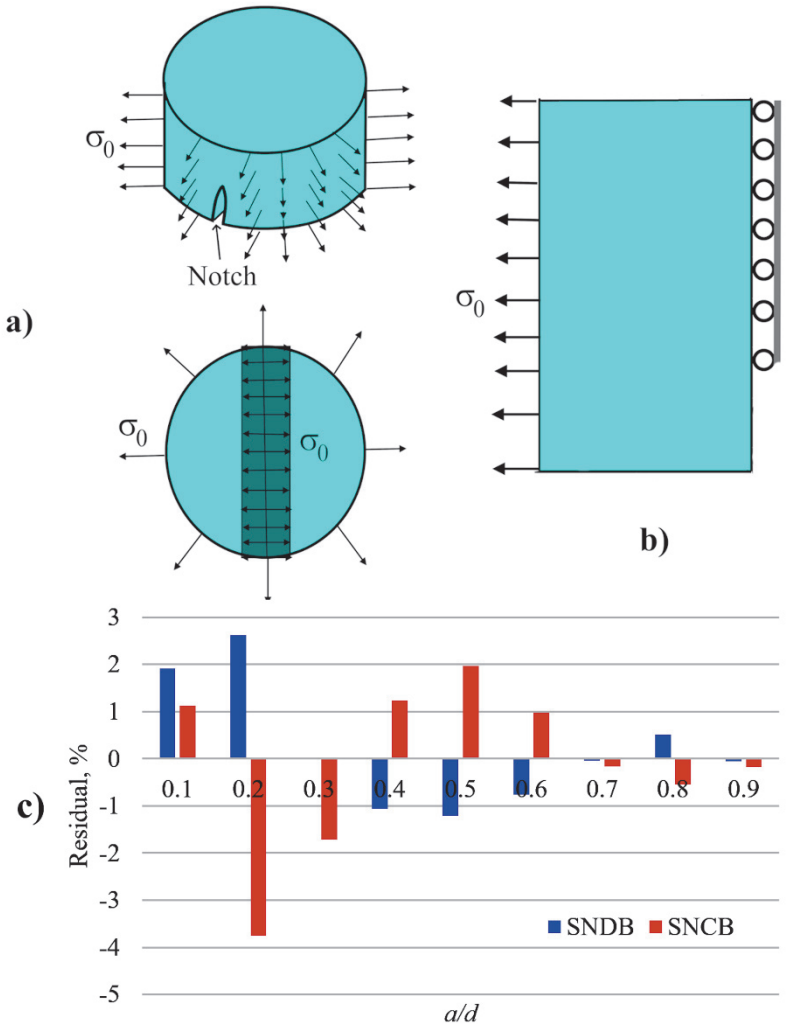

Figure 9: a) SNDB specimen under hoop stress and stress distribution b) SNCB specimen under tensile stress c) Eqns. (23) and (24) of residual values according to a/d ratios

IMPLEMENTATION OF THE COMPLIANCE METHOD AND THE PEAK LOAD METHOD TO SNDB SPECIMEN TESTS BY TUTLUOGLU AND KELES [14]

Experimental studies on grained composites such as rock have revealed that their fracture properties are highly affected by the maximum grain size and the uniaxial compressive strength of the material (σ_c). As a result, their behavior is characterized as being between brittle and ductile due to the internal structure of the material used. According to the TPM, the results of fracture test investigations performed on quasi-brittle materials have shown that there is a strong correlation between the uniaxial compressive strength and fracture toughness, while some properties related to the internal structure of the material, such as the maximum grain size, affect the $CTOD_c$ parameter.

Experimental and numerical studies on SNCB specimens were initially performed using Ankara andesite by Alkilicgil [15] and Tutluoglu and Keles [14]. For Ankara andesite, the elasticity modulus (E), the splitting tensile strength (f_{sp}), and Poisson's ratio were reported as 12334 ± 135 MPa, 7.00 ± 0.67 MPa and 0.15, respectively, by Tutluoglu and Keles [14]. The SNCB testing on cylindrical specimens with a diameter (D) of approximately 100 mm and a height (d) of approximately 50 mm was conducted for span/diameter ratios s/D = 0.6 and 0.7, and four different relative initiation notch lengths, $\alpha_0 = a_0/d$ = 0.1, 0.2, 0.3 and 0.4. Both P-displacement and P-$CMOD$ curves of the specimens were recorded in the fracture tests.

The geometrical properties (a_0, D, r, d, and s), the peak loads, and the critical $CMOD$ values ($CMOD_c$) at the peak load of successful test specimens are summarized in Tab. 2. In the specimen numbering in the first column of Tab. 2, the first

numbers (1, 2, 3, and 4) represent relative notch lengths corresponding to 0.1, 0.2, 0.3, and 0.4, while the next two-digit numbers (06 and 07) indicate the span/diameter ratios corresponding to 0.6 and 0.7. The last number refers to the number of successful test specimens for each notch length. A certain portion of the load-*CMOD* curves of SNDB specimens is illustrated separately for s/D = 0.6 and 0.7 in Fig. 10. Note that the P-CMOD curve of the specimen of 106-2, which was denoted with "*" in Tab. 2, is not presented in Fig. 10 since the curve was too noisy.

Some characteristic values ($\alpha_0=a_0/D$, $\sigma_{Nc}=P_c/(2Dd)$, C_i, and $C_s=CMOD_c/P_c$) computed for each specimen in Tab. 2 are summarized in the 2nd to 5th columns of Tab. 3 to apply the compliance method to SNDB specimens. In this table, the values of C_i were computed from the slope of the linear regression equation, which was determined by considering pairs of *P-CMOD* values up to approximately $P_c/2$ in the initial straight portion of the *P-CMOD* plots, as stated above. Accordingly, Young's modulus of the stone was determined from Eqns. (17) and (18) as follows:

$$E = \frac{\alpha_0}{2bC_i} V_1\left(\alpha_0\right) \tag{25}$$

The relative critical notch depth of each specimen in Tab. 3 was computed using the Newton method, assuming that the E value of the specimen remains constant for any notch depth, in accordance with the equivalent elastic crack approach:

$$\alpha_c = \alpha_0 \frac{C_s V_1\left(\alpha_0\right)}{C_i V_1\left(\alpha_c\right)} \tag{26}$$

The fracture quantities of the TPM (K_{Ic}^{s} and $CTOD_c$) were determined using Eqns. (1), (2), and (20) for each specimen in Tab. 3. As stated above, the unstable fracture toughness values of the TPM and the double-*K* are equivalent ($K_{Ic}^{s} = K_{Ic}^{un}$) and are therefore presented in a single column in Tab. 3. In Tab. 3, the mean values (μ), the standard deviation (σ), the coefficient of variation (C.V.), and the approximate 5% and 95% confidence limits ($\mu \pm 2\sigma$) of the fracture quantities and Young's modulus were also reported according to each span-to-diameter ratio. C.V. is beneficial when evaluating the variation among groups that exhibit notably different average mechanical properties, such as compressive strength while maintaining a consistent level of control. In many applications of concrete technology, a reasonable range for C.V. is 5% to 20%. It can be seen from Tab. 3 that the C.V. values of the TPM quantities, including E, $K_{Ic}^{s} = K_{Ic}^{un}$ and $CTOD_c$, are less than 20%. Furthermore, Tab. 3 shows that the value of E measured by Tutluoglu and Keles [14] falls within the confidence limits of that of the TPM. The crack extension values (Δa_c) were also reported for each specimen in the last two columns of Tab. 3. Tutluoglu and Keles [14] stated by using the numerical model that the Δa_c value was obtained as 3.92 ±0.86 mm for Ankara andesite, and this value also falls within the confidence limits of that of the TPM in Tab. 3.

The initial fracture toughness values of the double-*K* (K_{Ic}^{ini}) were computed using Eqns. (7), (8), and (23) and summarized in Tab. 3. In this procedure, to compute the lower limit stress of the cohesive stress distribution in Fig. 3a, the following linear expression proposed by Bažant [19], as depicted in Fig. 3b, was employed:

$$\sigma_s\left(CTOD_c\right) = f_t\left(1 - \frac{CTOD_c}{w_0}\right), \quad w_0 = \frac{2G_f}{f_t} \tag{27}$$

According to concrete design codes, the splitting tensile strength of quasi-brittle materials such as concrete is 1.5 times the direct tensile strength ($f_t=f_{sp}/1.5$). Based on this, the upper limit stress in Fig. 3a was taken as 4.667 MPa, which is close to the lower limit of the range given by Arioglu et al. [24] for andesite (5-11 MPa).

SNDB specimens were also analyzed using the peak-load method. The implementation of the peak-load method to a large number of specimens containing different notch depths $\left(a_c^1, a_c^2, \ldots a_c^n\right)$ is based on the following two basic equations:

$$K_I^i\left(\sigma_{Nc}^i, a_c^i\right) = K_{Ic}^s \qquad , i = 1, 2, ..., n$$
$$CTOD^i\left(\sigma_{Nc}^i, a_c^i\right) = CTOD_c \tag{28}$$

Here, n is the number of sets, i is the ith set and σ_{Nc}^i is the mean critical nominal strength of the ith set, which corresponds to the mean critical notch depth (a_c^i) of the ith set. By employing Eqns. (1) and (2), the K_{Ic}^s and $CTOD_c$ curves of specimens are initially plotted for each different notch depth to apply the method to the specimens in sets. Subsequently, the mean K_{Ic}^s and $CTOD_c$ curves, along with the standard deviation curve based on Eqn. (6), are plotted. Consequently, the fracture quantities of the material can be determined from the abscissa and ordinate of the point corresponding to the minimum standard deviation on the mean curve.

Fig. 11 illustrates the implementation of the peak load method for SNDB specimens with Ankara andesite. In these figures, the K_{Ic}^s and $CTOD_c$ plots of the SNDB specimens with s/D=0.6 are shown at the top, while those of the SNDB specimens with s/D=0.7 are at the bottom. The standard deviation plots based on Eqn. (6) are presented in the middle. In conclusion, the fracture quantities of the stone material were calculated from the s_{min} values, which correspond to the minimum standard deviations, as depicted in Fig. 11. This figure demonstrates a strong correlation between both fracture quantities of Ankara andesite despite using SNDB specimens with two different s/D ratios. Note that the E value measured by Tutluoglu and Keles [14] was used in this analysis. In Tab. 4, the relative critical notch depths (α_c) and the crack extension values (Δa_c) of the stone material are reported for each α_0 and each s/D ratio. Using Eqns. (7), (8), and (23), the parameters of initiation fracture toughness of the double-K model, computed according to results of the peak load method, are also summarized in Tab. 4.

No	a_0 mm	D mm	r mm	d mm	s mm	P_c N	$CMOD_c$ mm
106-1	6.5	101.74	50.9	50.1	61.76	26020	0.0347
*106-2	5.5	101.02	50.3	49.6	60.62	24549	0.0299
106-3	5	100.98	50.5	50.1	61.02	21712	0.0334
206-1	10	101.83	50.9	48	61.82	15882	0.035
206-2	9.75	101.8	50.9	48.1	61.78	16346	0.038
206-3	9.75	101.71	50.8	47.8	61.7	16535	0.0414
306-1	15.63	101.68	50.9	50.1	61.72	15728	0.0471
306-2	15.25	101.68	50.8	50	61.7	14456	0.0443
406-1	20.5	101.65	50.8	50.5	61.6	10326	0.0488
406-2	20.25	101.68	50.8	50.9	61.7	12250	0.0532
406-3	20	101.43	50.7	50	61.32	12431	0.0513
107-1	5.5	101.85	50.9	50.4	71.84	18337	0.0341
107-2	5.5	101.48	50.8	50.2	71.52	20310	0.0352
207-1	10.5	101.67	50.8	49.7	71.68	13649	0.0419
207-2	10.75	101.81	50.9	50.2	71.8	15058	0.045
207-3	9.75	101.8	50.9	50.4	71.8	15568	0.0398
307-2	15.38	101.77	50.9	51.1	71.78	12917	0.0488
307-3	15.5	101.68	50.8	50	71.66	12150	0.0548
407-2	20	101.7	50.9	51.3	71.74	9596	0.048
407-3	21	101.76	50.9	51.2	71.76	10377	0.0573

Table 2: Test Results of SNDB specimens by Alkilicgil [15].

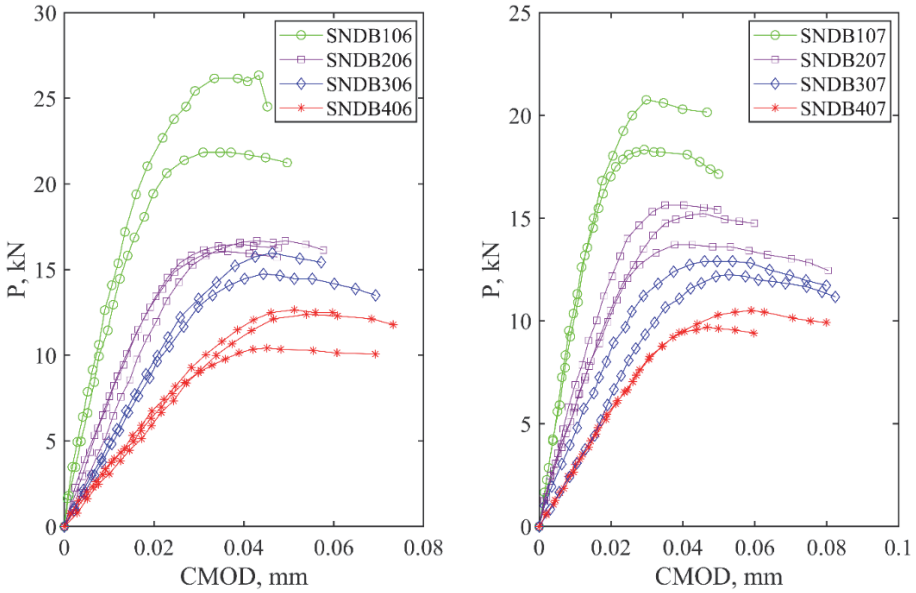

Figure 10: Load-CMOD plots of SNDB tests by Alkilicgil [15].

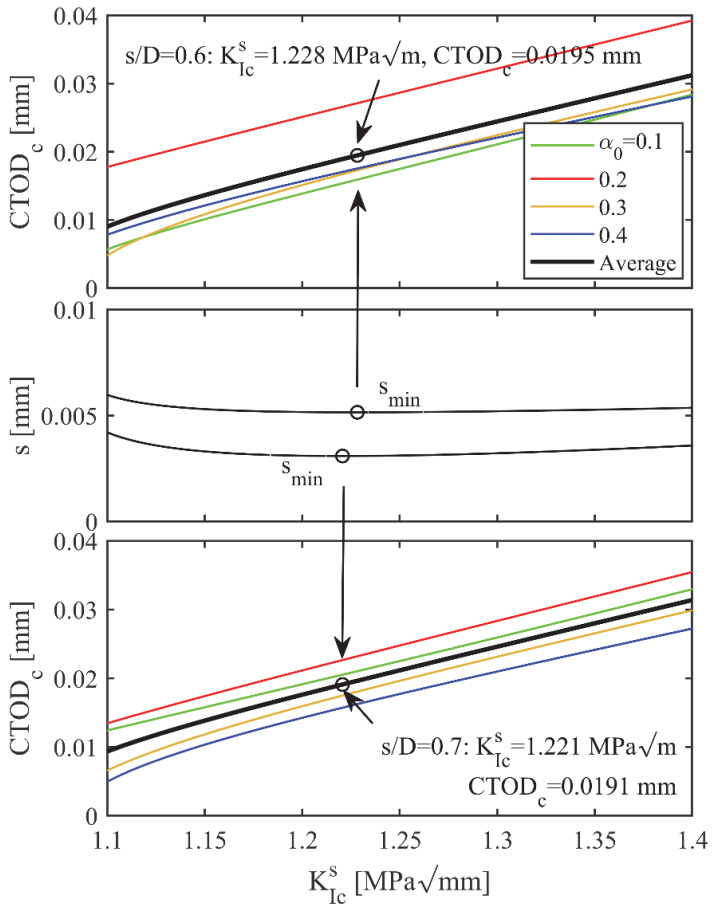

Figure 11: Implementation of TPM to SNDB specimens experimented by Alkilicgil [15].

No	α_0	σ_{Nc} MPa	$C_i\times10^{-6}$ mm/N	$C_s\times10^{-6}$ mm/N	E MPa	α_c	$K_{Ic}^{s}=K_{Ic}^{un}$ MPa√m	$CTOD_c$ mm	K_{Ic}^{ini} MPa√m	Δa_c mm
106-1	0.130	2.552	0.687	1.334	19891	0.234	1.579	0.0210	0.640	5.21
106-3	0.100	2.146	0.774	1.538	13581	0.190	1.201	0.0214	0.360	4.51
206-1	0.208	1.625	1.278	2.204	18015	0.314	1.217	0.0173	0.340	5.09
206-2	0.203	1.669	1.338	2.325	16665	0.309	1.201	0.0191	0.332	5.10
206-3	0.204	1.701	1.717	2.504	13094	0.275	1.128	0.0180	0.411	3.39
306-1	0.312	1.544	2.039	2.995	19313	0.392	1.396	0.0166	0.632	4.01
306-2	0.305	1.422	2.192	3.064	17365	0.375	1.227	0.0149	0.528	3.50
406-1	0.406	1.006	2.929	4.726	21144	0.501	1.263	0.0152	0.476	4.80
406-2	0.398	1.183	3.282	4.343	18138	0.455	1.289	0.0134	0.682	2.90
406-3	0.400	1.226	2.825	4.127	21346	0.476	1.414	0.0147	0.699	3.80
mean=μ					17855		1.292	0.0172	0.510	4.23
Std=σ					2828		0.134	0.0027		0.82
C.V.					0.158		0.104	0.159		19.43
μ–2σ					12199		1.023	0.0117		2.59
μ+2σ					23511		1.560	0.0226		5.87
107-1	0.109	1.786	0.885	1.860	15482	0.215	1.267	0.0221	0.362	5.34
107-2	0.110	1.993	0.938	1.733	14720	0.193	1.337	0.0213	0.505	4.17
207-1	0.211	1.351	1.644	3.070	17196	0.333	1.266	0.0216	0.323	6.06
207-2	0.214	1.473	1.706	2.988	16820	0.324	1.355	0.0222	0.433	5.52
207-3	0.193	1.517	1.419	2.556	17935	0.305	1.335	0.0208	0.403	5.64
307-2	0.301	1.242	2.142	3.778	21031	0.418	1.475	0.0204	0.530	5.98
307-3	0.310	1.195	3.349	4.510	14070	0.372	1.238	0.0174	0.583	3.10
407-2	0.390	0.920	3.405	5.002	20336	0.468	1.264	0.0142	0.544	4.00
407-3	0.410	0.996	3.557	5.522	21469	0.497	1.501	0.0170	0.719	4.45
mean=μ					17673		1.338	0.0197	0.489	4.92
Std=σ					2746		0.094	0.0028		1.03
C.V.					0.155		0.071	0.142		20.87
μ–2σ					12182		1.149	0.0141		2.87
μ+2σ					23164		1.526	0.0253		6.97

Table 3: Results of the compliance-based analysis for each data

Group	s/D	α_0	σ_{Nc} MPa	$K_{Ic}^{s}=K_{Ic}^{un}$ MPa√m	$CTOD_c$ mm	α_c	K_{Ic}^{ini} MPa√m	Δa_c mm
106	0.6	0.113	2.383	1.228	0.0195	0.174	0.512	3.06
206	0.6	0.205	1.665			0.281	0.461	3.65
306	0.6	0.308	1.483			0.368	0.589	3.00
406	0.6	0.401	1.138			0.461	0.616	3.03
107	0.7	0.109	1.890	1.221	0.0191	0.172	0.485	3.17
207	0.7	0.206	1.447			0.271	0.504	3.26
307	0.7	0.305	1.218			0.364	0.585	2.98
407	0.7	0.400	0.958			0.456	0.628	2.87

Table 4: Results of the TPM-based analysis for grouped data of SNDB specimen.

Statistical comparison of different fracture analysis methods used in SNDB specimens

When comparing Tabs. 3 and 4, considering basic statistical parameters such as the mean value and the 5% and 95% confidence limits, it can be concluded that there is no significant difference between the compliance method and the peak load method, based on the fracture quantities of Ankara andesite. Similarly, when the critical crack extension values of TPM in Tab. 3 are compared with the values in the numerical model proposed by Tutluoglu and Keles [14], it can be concluded that there is no significant difference between both models, based on the FPZ depth.

An important feature of statistics is its ability to facilitate the comparison of two data sets, allowing for the assessment of the likelihood that they differ significantly from one another. For this reason, two comparison tests are widely employed to determine whether they are potentially derived from the same sample population. These are the Student's t-test, which compares the means of samples, and the F-test, which compares the standard deviations of samples. The expressions for these tests can be given for paired comparisons as follows:

$$t_{calc} = \frac{\left|\mu_1 - \mu_2\right|}{\sqrt{\sum_{i=1}^{n}\left(d_i - \delta\right)^2 \Big/ n-1}}\sqrt{n} \tag{29}$$

$$F_{calc} = \frac{\sigma_1^2}{\sigma_2^2} \tag{30}$$

In Eqn. (29), μ_1 and μ_2 are the means of the first and the second data sets for the number of data points n, respectively, while d_i and δ represent the differences for each pair of data and the mean of d_i. In Eqn. (30), σ_1 and σ_2 are the standard deviations of the first and the second data sets, respectively, provided that $\sigma_1 > \sigma_2$. In addition to assuming that the populations are normally distributed in the two statistical methods defined above, the Student's t-test assumes that both populations have the same variance, while the F-test assumes that the populations have the same means.

The aforementioned statistical test methods can also be employed to compare two different testing or analysis methods in any process. Moreover, the F-test can be utilized to assess the precision of a newly developed method based on a method whose accuracy is already known. In this study, a statistical comparison of SNDB specimens with different notch lengths was conducted between the compliance method proposed by RILEM and the peak load method, which is commonly employed in concrete fracture tests. For this comparison, the reciprocal K_{Ic}^{ini} parameters computed for each notch depth in Tab. 3 (based on compliance analysis) and Tab. 4 (based on the peak load method) were utilized, as this parameter is based on both $K_{Ic}^{s} = K_{Ic}^{un}$ and $CTOD_c$ parameters.

The comprehensive details of the statistical analysis are reported in Tab. 5. In this context, SNDB1, SNDB2, SNDB3, and SNDB4 represent specimens corresponding to relative notch lengths of 0.1, 0.2, 0.3, and 0.4, respectively. Prior to the comparative analysis, the normality of the dataset was verified using the Shapiro-Wilk test. Despite the small sample size (n=4), all p-values exceeded the 0.05 threshold, justifying the use of parametric tests. The values of t_{calc} and F_{calc} were calculated using Eqns. (30) and (31), respectively, while their corresponding values from statistical tables ($t_{n-1,0.025}$ and $F_{0.05,\,n-1,\,n-1}$, where n-1 is the degrees of freedom) were determined for the 5% significance level in this study. Note that since means are being compared, Student's t-test was performed as a two-tailed test (0.05/2=0.025). To provide a robust comparison, 95% Confidence Intervals for the means were calculated for each group. The overlap between the confidence intervals of the two methods suggests a strong similarity in the results. Furthermore, to address the practical significance of the results, the effect size (Hedges' g) and post-hoc power were computed. For both geometries, the effect sizes were found to be negligible ($g \leq 0.10$), and the achieved power was low. These indicators demonstrate that the difference between the compliance and peak load methods is virtually non-existent for the tested material. Accordingly, it can be concluded from Tab. 5 that there is no significant difference between the compliance and peak load methods regarding initiation fracture toughness parameters, as the computed values are less than their corresponding values from statistical tables. Consequently, considering the discussion above, it can be concluded that the peak load method has the same level of precision as the compliance method proposed by RILEM.

In this study, another statistical analysis was conducted to compare the compliance method and the numerical model proposed by Tutluoglu and Keles [14]. By using the FEA, Tutluoglu and Keles [14] simulated the SNDB specimens with $d=(D/2)=50$ mm and $s/d=0.3$ and 0.35 for $a_0/d=0.1$, 0.2, 0.3 and 0.4. In this analysis, the mean peak loads were utilized

for each a_0/d and s/d. According to this, stress distributions along the notch line (σ_{xx}) were determined. Subsequently, the FPZ depths (Δa_c) in front of the notch were determined at σ_{Nc}/σ_{xx}=1. Consequently, the value of Δa_c was determined as 3.92±0.86 mm.

For the statistical comparison of both approaches, by considering the above-mentioned numerical analysis, a total of 8 fracture toughness values (K_{Ic}^{ref}) were computed based on Eqn. (1) using the values of $a_c=a_0$+3.92 mm (a_0=5, 10, 15, and 20 mm) and corresponding to the mean values of σ_{Nc} for s/d= 0.3 and 0.35. In response, a total of 19 fracture toughness values ($K_{Ic}^{s} = K_{Ic}^{un}$) determined according to the compliance method were utilized for statistical comparison.

The t-test based on Eqn. (29) is valid for paired comparisons. If the number of data to be compared is different, the following relation is used for the t-test:

$$t_{calc} = \frac{\left|\mu_1 - \mu_2\right|}{\sqrt{\frac{\left(n_1-1\right)\sigma_1^2 + \left(n_2-1\right)\sigma_2^2}{n_1+n_2-2}}\sqrt{\frac{1}{n_1}+\frac{1}{n_2}}} \tag{31}$$

s/D		0.6			0.7	
Method	Compliance	Peak Load	d_i	Compliance	Peak Load	d_i
SNDB1	0.500	0.512	-0.012	0.434	0.485	-0.052
SNDB2	0.361	0.461	-0.100	0.386	0.504	-0.118
SNDB3	0.580	0.589	-0.009	0.557	0.585	-0.029
SNDB4	0.619	0.616	0.003	0.632	0.628	0.003
Descriptive Statistics						
n		4			4	
μ, δ	0.515	0.545	-0.030	0.502	0.551	-0.049
σ	0.114	0.071	0.048	0.112	0.067	0.051
95% Confidence Interval for Mean	[0.334, 0.696]	[0.324, 0.680]		[0.432, 0.658]	[0.444, 0.658]	
Normality Check						
Shapiro-Wilk (p)	0.608	0.761		0.516	0.596	
Result	Normal	Normal		Normal	Normal	
Hypothesis Testing						
t_{calc}	1.24 (p>0.05)			1.89 (p>0.05)		
$t_{3,0.025}$	2.35			2.35		
Result	t_{calc} = 1.24 < $t_{3,0.025}$=2.35			t_{calc} = 1.89 < $t_{3,0.025}$ = 2.35		
F_{calc}	2.58 (p>0.05)			2.77 (p>0.05)		
$F_{0.05,3,3}$	9.28			9.28		
Result	F_{calc} = 2.58 < $F_{0.05,3,3}$=9.28			F_{calc} = 2.77 < $F_{0.05,3,3}$ = 9.28		
Effect Size (Hedges' g)	0.10 (Negligible)			0.08 (Negligible)		
Achieved Power (1-β)	0.056			0.054		
There is not a significant difference between initiation fracture toughness.						

Table 5: Statistical comparison based on t-test and F-test for K_{Ic}^{ini} in this study

Here, n_1 and n_2 are the numbers of data in samples. Details of the second statistical comparison conducted are summarized in Tab. 6. Prior to applying the comparison formulas, the normality of the datasets was verified via the Shapiro-Wilk test. Despite the unbalanced sample sizes (n_1=19 vs. n_2=8), the data followed a normal distribution (p > 0.05), validating the

application of parametric tests. In this table, the values of t_{calc} and F_{calc} were computed utilizing Eqns. (31) and (30), respectively, while their corresponding values from statistical tables ($t_{n1+n2-2,0.025}$ and $F_{0.05,\,n1-1,\,n2-1}$) were determined for the 5% significance level in this analysis. To further substantiate the comparison, 95% Confidence Intervals and the effect size (Hedges' g) were calculated. Although a medium effect size ($g = 0.66$) was observed, the 95% Confidence Intervals exhibited overlap, suggesting consistency between the datasets. Accordingly, it can be concluded from Tab. 6 that there is no significant difference between the compliance method and the numerical method proposed by Tutluoglu and Keles [14] regarding non-linear fracture toughness parameters, as the determined test statistics remain below their corresponding tabular limits.

IMPLEMENTATION OF THE PEAK LOAD METHOD FOR SNCB SPECIMEN TESTS ON ELAZIG LIMESTONE [14]

Experimental program

Based on the above statistical test analysis, it was concluded that there is no significant difference between the compliance method and the peak load method in determining the nonlinear fracture quantities of rock materials. Based on this conclusion, the fracture mechanics analysis of Elazig limestone was performed utilizing the peak load method. On the other hand, beams and SNCB specimens containing notch depths were fabricated from Elazig limestone to validate the results. To determine the mechanical properties of the stone, such as compressive strength, tensile strength, and Young's modulus, cubes and beams without notches were also prepared.

Compression cubes, as illustrated in Fig. 12a, were subjected to monotonic loading at a rate of 3.00 kN/s in a concrete hydraulic compression press with a 2000 kN actuator. The average compressive strength of three 70 mm cubes was 190.4 MPa. Durmekova et al. [25] performed tests on many rock cylindrical and prismatic specimens and concluded that the ratio of cubical strength to cylindrical strength was 1.15. Accordingly, the cylindrical strength of the rock with a diameter of 70 mm is 165.6 MPa. Consequently, when the cylindrical strength with a 70 mm diameter is transformed to the cylindrical strength with a 50 mm diameter, according to the size effect formula proposed by Hoek and Brown, where $\sigma_c^d = \sigma_c / (50/d)^{0.18}$, where σ_c^d and σ_c represents the strengths of specimens with diameters d and 50 mm (standard), respectively, the standard strength value of Elazig Limestone was obtained as σ_c=175.9 MPa. Note that the test data for limestone fit well with the formula by Hoek and Brown. The Young's modulus of the rock (E) was determined by utilizing the following power formula proposed by Arioglu et al. [24]:

$$E = 0.76\sigma_c^{0.72} \tag{32}$$

Here, σ_c is in MPa, while E is in GPa. The above empirical formula, with a correlation coefficient of 0.812, was determined based on 119 different limestone test data. Accordingly, the value of E for the rock was evaluated as 52.7 GPa for the standard strength.

The average bending strength (f_r) of three beams (width × depth × length = 50 × 50 × 200 mm) tested under a loading span of 125 mm, whose failures are shown in Fig. 12a, was obtained as 11.468 MPa using a compression press with a 100 kN actuator. Concrete design codes suggested that the direct tensile strength of quasi-brittle materials such as concrete should be taken as half of the bending tensile strength (f_t=f_r/2). According to this, in the following analysis, the tensile strength of the stone was assumed to be 5.734 MPa, which is within the range given by Arioglu et al. [24] for limestone (4-7 MPa).

The beams were loaded at three points with a span/depth=2.5 (Fig. 12b), while the SNCB specimens were subjected to three-point bending with a span-to-diameter ratio of 0.8 (Fig. 12d). All specimens containing a notch were fractured using the compression press with a 100 kN actuator, with the time to reach the peak load set to 3 minutes (± 30 seconds).

Crack patterns at the failure of beams and SNCB specimens containing a notch are illustrated in Figs. 12c and 12e, respectively. The dimensions of section sizes (b and d) and the peak load values (P_c) of the notched beam and SNCB specimens were summarized in Tab. 7 according to the initial notch depths (a_0). In this table, "B" and "SNCB" refer to the specimen types for beam and SNCB, respectively. In the specimen numbering in the first column of Tab. 6, the first numbers (1, 2, and 3) refer to relative notch lengths corresponding to 0.3, 0.4, and 0.5, while the last number illustrates the number of successful test specimens for each notch length.

No	$K_{Ic}^{s} = K_{Ic}^{un}$ MPa√m	K_{Ic}^{ref} MPa√m
106-1	1.579	1.265
106-3	1.201	
206-1	1.217	
206-2	1.201	1.068
206-3	1.128	
306-1	1.396	1.269
306-2	1.227	
406-1	1.263	
406-2	1.289	1.314
406-3	1.414	
107-1	1.267	1.201
107-2	1.337	
207-1	1.266	
207-2	1.355	1.168
207-3	1.335	
307-2	1.475	1.276
307-3	1.238	
407-2	1.264	1.357
407-3	1.501	
Descriptive Statistics		
n	19	8
μ	1.313	1.240
σ	0.116	0.091
95% Confidence Interval for Mean	[1.257, 1.369]	[1.164, 1.316]
Normality Check		
Shapiro-Wilk (p)	0.285	0.812
Result	Normal	Normal
Hypothesis Testing		
t_{calc}	1.58 (p>0.05)	
$t_{25,0.025}$	1.71	
Result	t_{calc} = 1.58 < $t_{25,\,0.025}$=1.71	
F_{calc}	1.63 (p>0.05)	
$F_{0.05,18,7}$	3.47	
Result	F_{calc} = 1.63 < $F_{0.05,\,18,7}$=3.47	
Effect Size (Hedges' g)	0.66 (Medium)	
Achieved Power (1-β)	0.34	
There is not a significant difference between fracture toughness.		

Table 6: Statistical comparison based on t-test and F-test between this study and Tutluoglu and Keles [14] for non-linear fracture toughness.

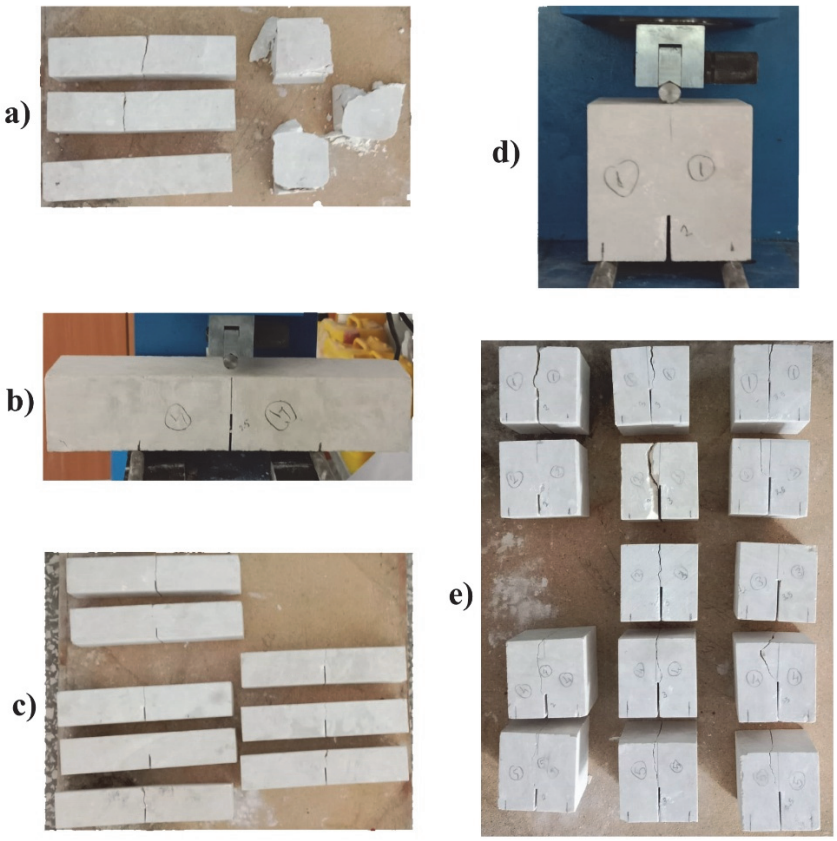

Figure 12: Test details of limestone specimens a) fractured flexural and compressive specimens b) notched beam test setup c) fractured notched beams d) SNCB specimen test setup e) fractured SNCB specimens.

As stated above, the peak load method based on TPM is an optimization-based technique since the number of unknowns (three or more distinct specimens must be tested to ensure statistically valid results) is greater than the number of equations (Eqns. (1) and (2)). The objective function of the optimization problem is to minimize Eqn. (6), while the constraints of the problem are the critical crack lengths, which must be greater than initial crack lengths and smaller than specimen depth as detailed below.

Fig. 13 indicates the implementation of the peak load method to beams and SNCB specimens with Elazig limestone. The K_{Ic}^{s} and $CTOD_c$ plots of the beams are demonstrated at the top, and those of the SNCB specimens are at the bottom, while the s-K_{Ic}^{s} plots based on Eqn. (6) are illustrated in the middle in Fig. 13. For the dimensionless functions used in drawing the K_{Ic}^{s} and $CTOD_c$ plots, Eqns. (3)-(5) were used for beams, while Eqns. (16), (19), and (21) derived in this study were employed for SNCB specimens. This figure shows that there is a strong correlation between the unstable fracture toughness of Elazig limestone for both specimen types. To compute the initiation fracture toughness based on the double-K, Eqns. (9) and (27) were employed for beams and SNCB specimens, respectively. The fracture quantities corresponding to each α_0 value were reported for two different bending specimens in Tab. 8.

In the last column of Tab. 8, the relative crack extension values ($\Delta\alpha_c$) are also presented for each specimen and each α_0 value. These values demonstrate that the effect of the FPZ on the fracture quantities of rocks cannot be ignored, as it is in other quasi-brittle civil engineering materials such as concrete and asphalt concrete. Although both specimen types are subjected to three-point bending loading, the $\Delta\alpha_c$ values of beams are smaller than those of SNCB specimens. The most important reason for this is that SNCB specimens behave like deep beams, where the depth of the compression zone is larger than that of the beam under three-point bending loading. On the other hand, it is well known that the depth of crack extension at the peak load is not a fracture parameter and varies depending on specimen type and specimen size in quasi-brittle materials [2].

Specimen	b mm	d mm	a_0 mm	P_c kN
B11	51.6	50.67	14.93	3.51
B12	50.29	50.61	15.17	3.7
B21	51.01	50.76	20.6	2.7
B22	51.01	50.93	20.21	2.83
B23	50.69	50.54	20.16	2.3
B31	50.75	50.71	25	1.73
B32	50.52	50.97	24.34	2.08
B33	50.39	50.81	25.69	1.73
SNCB11	70.91	71.05	20.75	29.49
SNCB12	71.3	71.23	20.91	29.81
SNCB13	70.68	71.37	20.98	29.2
SNCB14	71.17	71.38	20.82	29.03
SNCB21	71.34	71.61	31.7	18.36
SNCB22	70.8	71.53	31.56	13.97
SNCB23	71.71	71.36	31.45	14.45
SNCB24	71.25	71.19	31.08	17.65
SNCB25	71.27	71.45	31.4	16.48
SNCB31	72.06	71.22	35.54	12.93
SNCB32	71.48	70.99	35.5	12.71
SNCB33	71.07	71.45	37.16	13.05
SNCB34	71.15	71.29	35.76	15.31
SNCB35	70.92	71.21	35.84	13.72

Table 7: Test results of beams and SNCB specimens tested in this study

Group	s/d	α_0	σ_{Nc} MPa	$K_{Ic}^{s} = K_{Ic}^{un}$ MPa√m	$CTOD_c$ mm	α_c	K_{Ic}^{ini} MPa√m	$\Delta\alpha_c$
B1	2.5	0.297	2.383	2.260	0.0188	0.538	0.939	0.241
B2	2.5	0.401	1.483			0.623	0.924	0.222
B3	2.5	0.497	1.138			0.696	0.893	0.199
SNCB1	0.8	0.293	1.890	2.244	0.0158	0.432	1.326	0.139
SNCB2	0.8	0.440	1.447			0.605	0.916	0.165
SNCB3	0.8	0.505	0.958			0.659	0.872	0.154

Table 8: Results of fracture analysis for grouped data of Elazig limestone.

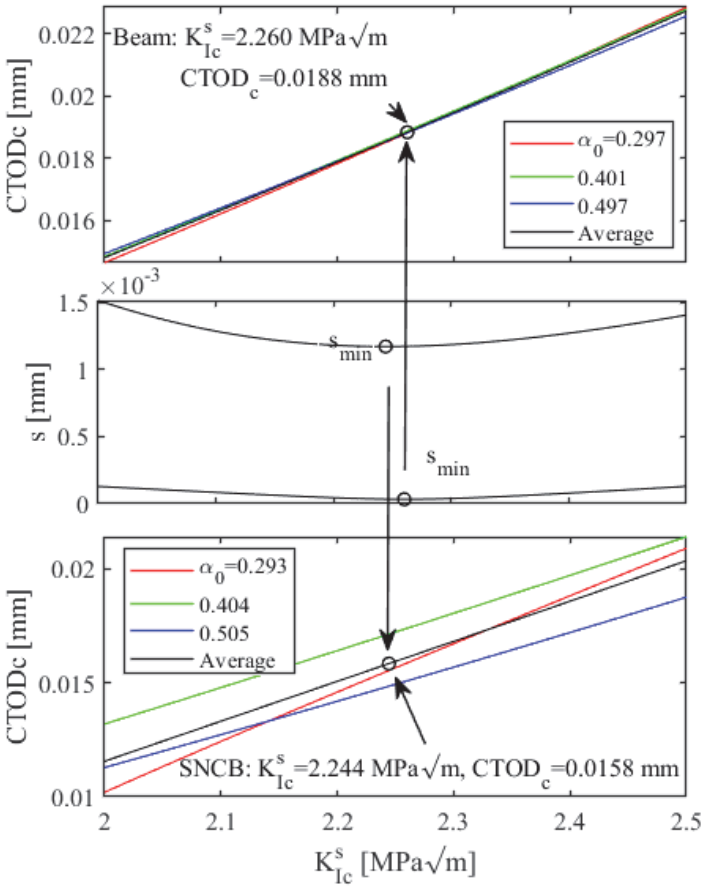

Figure 13: Implementation of TPM to beams and SNCB specimens tested in this study.

Conclusion

Nonlinear fracture models, frequently applied in the examination of concrete fracture, were utilized in this study to evaluate the fracture quantities of quasi-brittle SNDB and SNCB specimens made from rock materials. The results of this investigation are summarized below:

1) The examination of rock SNDB specimens with a depth/diameter ratio of 0.5, documented in the literature, utilized both the compliance method and the peak load method, revealing a significant correlation between the two approaches. This has previously been observed in other quasi-brittle materials such as concrete and asphalt concrete. It is emphasized that the most important advantage of the peak-load method is that it does not require sophisticated test equipment, unlike the compliance method, to determine the fracture quantities of the materials.
2) Another statistical comparison based on the t-test and the F-test was conducted for the compliance method based on the TPM and the numerical method based on the FEA proposed by Tutluoglu and Keles [14]. It was revealed that there was a significant correlation between the two methods according to both the means and the variances.
3) The fracture tests of comparative tests on beams and SNCB specimens reveal that the fracture quantities of rocks based on the TPM and the double-*K* model can easily be estimated using SNCB specimen tests, so specimens of differing sizes are unnecessary. On the other hand, the LEFM expressions derived for cubical specimens containing an edge notch can also be used for square prismatic specimens containing an edge notch subjected to a bending load.
4) The primary benefits of cylindrical and cubical specimens containing an edge notch, examined in this study, are their lightness and compactness compared to beams. Furthermore, in the determination of the fracture quantities of rocks, the use of these specimens, facilitated by core drilling, enables the extraction of materials from rock formations, providing significant benefits.
5) The CCI technique is not as commonly used as the J-integral approach and is not integrated into many commercial finite element method software. However, the implementation of the CCI technique is notably more

straightforward compared to the J-integral method. In the three-dimensional applications conducted in this study, the results of the CCI technique were satisfactorily consistent with the J-integral approach. So much so that even solutions with eight-node solid elements yielded sufficiently satisfactory results. Eight-node solid elements are the only element type used in commercial programs such as SAP2000, which is commonly used in civil engineering.

ACKNOWLEDGMENTS

This study was carried out within the scope of the Firat University Scientific Research Projects program (FUBAP) with the Research Project number of MF.24.08. We gratefully acknowledge the financial support provided by FUBAP.

REFERENCES

[1] Irwin, G.R. (1957). Analysis of Stresses and Strains Near the End of a Crack Traversing a Plate, J. Appl. Mech., 24(3), pp. 361–4, Doi: 10.1115/1.4011547.

[2] Jenq, Y., Shah, S.P. (1985). Two Parameter Fracture Model for Concrete, J. Eng. Mech., 111(10), pp. 1227–41, Doi: 10.1061/(ASCE)0733-9399(1985)111:10(1227).

[3] Bažant, Z.P., Kazemi, M.T. (1990). Determination of fracture energy, process zone length and brittleness number from size effect, with application to rock and concrete, Int. J. Fract., 44(2), pp. 111–31, Doi: 10.1007/BF00047063.

[4] Xu, S., Reinhardt, W.H., Wu, Z., Zhao, Y. (2003). Comparison between the Double-K Fracture Model and the Two Parameter Fracture Model, Otto-Graf-Journal, 14, pp. 131–57.

[5] ISRM. (1988). Suggested methods for determining the fracture toughness of rock, Int. J. Rock Mech. Min. Sci. Geomech. Abstr., 25(2), pp. 71–96, Doi: 10.1016/0148-9062(88)91871-2.

[6] Bažant, Z.P., Gettu, R., Kazemi, M.T. (1991). Identification of nonlinear fracture properties from size effect tests and structural analysis based on geometry-dependent R-curves, Int. J. Rock Mech. Min. Sci. Geomech. Abstr., 28(1), pp. 43–51, Doi: 10.1016/0148-9062(91)93232-U.

[7] Ouyang, C., Tang, T., Shah, S.P. (1996). Relationship between fracture parameters from two parameter fracture model and from size effect model, Mater. Struct., 29(2), pp. 79, Doi: 10.1007/BF02486197.

[8] Ince, R. (2021). Utilization of splitting strips in fracture mechanics tests of quasi-brittle materials, Arch. Appl. Mech., 91(6), pp. 2661–79, Doi: 10.1007/s00419-021-01913-5.

[9] Zegeye, E., Le, J.-L., Turos, M., Marasteanu, M. (2012). Investigation of size effect in asphalt mixture fracture testing at low temperature, Road Mater. Pavement Des., 13(sup1), pp. 88–101, Doi: 10.1080/14680629.2012.657064.

[10] Ince, R., Yalcin, E., Yilmaz, M. (2024). Quantifying nonlinear fracture parameters in bituminous SCB specimens: A compliance-based approach, Case Stud. Constr. Mater., 21, pp. e03437, Doi: 10.1016/j.cscm.2024.e03437.

[11] Wei, M.-D., Dai, F., Xu, N.-W., Zhao, T., Liu, Y. (2017). An experimental and theoretical assessment of semi-circular bend specimens with chevron and straight-through notches for mode I fracture toughness testing of rocks, Int. J. Rock Mech. Min. Sci., 99, pp. 28–38, Doi: 10.1016/j.ijrmms.2017.09.004.

[12] Guo, Z., Li, J., Song, Y., He, C., Zhang, F. (2021). The Size Effect and Microstructure Changes of Granite after Heat Treatment, Adv. Mater. Sci. Eng., 2021, pp. 1–14, Doi: 10.1155/2021/9958255.

[13] Ince, R. (2025). Using SCB specimens to quantify nonlinear fracture characteristics in concrete and rock materials, Eng. Fract. Mech., 318, pp. 110951, Doi: 10.1016/j.engfracmech.2025.110951.

[14] Tutluoglu, L., Keles, C. (2011). Mode I fracture toughness determination with straight notched disk bending method, Int. J. Rock Mech. Min. Sci., 48(8), pp. 1248–61, Doi: 10.1016/j.ijrmms.2011.09.019.

[15] Alkılıçgil, C. (2006).Development of A New Method for Mode I Fracture Toughness Test on Disc Type Rock Specimens. M.Sc. Thesis, Middle East Technical University, 2006.

[16] Tutluoglu, L., Karatas Batan, C., Aliha, M.R.M. (2022). Tensile mode fracture toughness experiments on andesite rock using disc and semi-disc bend geometries with varying loading spans, Theor. Appl. Fract. Mech., 119, pp. 103325, Doi: 10.1016/j.tafmec.2022.103325.

[17] Ayatollahi, M.R., Aliha, M.R.M. (2007). Wide range data for crack tip parameters in two disc-type specimens under mixed mode loading, Comput. Mater. Sci., 38(4), pp. 660–70, Doi: 10.1016/j.commatsci.2006.04.008.

[18] Tang, T., Ouyang, C., Shah, S.P. (1996). Simple Method for Determining Material Fracture Parameters From Peak Loads, ACI Mater. J., 93(2), pp. 147–57, Doi: 10.14359/1413.
[19] Bažant, Z.P. (2002). Concrete fracture models: testing and practice, Eng. Fract. Mech., 69(2), pp. 165–205, Doi: 10.1016/S0013-7944(01)00084-4.
[20] Tada, H., Paris, P.C., Irwin, G.R. (2000). The Stress Analysis of Cracks Handbook, Third Edition, ASME Press.
[21] Ince, R. (2012). Determination of the fracture parameters of the Double-K model using weight functions of split-tension specimens, Eng. Fract. Mech., 96, pp. 416–32, Doi: 10.1016/j.engfracmech.2012.08.024.
[22] Maiti, S.K. (2015). Fracture mechanics: fundamentals and applications, Cambridge, Cambridge University Press.
[23] Tang, T. (1994). Effects of Load-Distributed Width on Split Tension of Unnotched and Notched Cylindrical Specimens, J. Test. Eval., 22(5), pp. 401, Doi: 10.1520/JTE12656J.
[24] Arioglu, E., Arioglu, N., Yilmaz, A.O. (2006). Concrete Aggregates, İstanbul, Evrim Publishers (in Turkish).
[25] Durmeková, T., Bednarik, M., Dikejová, P., Adamcová, R. (2022). Influence of specimen size and shape on the uniaxial compressive strength values of selected Western Carpathians rocks, Environ. Earth Sci., 81(9), pp. 247, Doi: 10.1007/s12665-022-10373-1.